OPTIMIZATION OF ND:YAG LASER BEAM AND PROCESS PARAMETERS FOR QUALITY MICROMACHINING OF MONOCRYSTALLINE SILICON

TITUS MURWA MULEMBO

MASTER OF SCIENCE
(Mechatronic Engineering)

JOMO KENYATTA UNIVERSITY OF
AGRICULTURE AND TECHNOLOGY

2014

Optimization of Nd:YAG Laser beam and Process Parameters for Quality Micromachining of Monocrystalline Silicon

Titus Murwa Mulembo

A thesis submitted in partial fulfillment for the of Degree of Master of Science in Mechatronic Engineering in the Jomo Kenyatta University of Agriculture and Technology

2014

DECLARATION

This thesis is my original work and has not been presented for a degree in any other University.

Signature:.. Date...................

Titus Murwa Mulembo

This thesis has been submitted with our approval as the University Supervisors.

Signature:.. Date...................

Eng. Prof. B. W. Ikua
JKUAT, Kenya

Signature:.. Date...................

Dr. J. N. Keraita
DeKUT, Kenya

Signature:.. Date...................

Dr. A. Niyibizi
DeKUT, Kenya

DEDICATION

This work is dedicated to my family for the great support they gave me during the course of the research.

ACKNOWLEDGEMENT

I am greatly indebted to my supervisors Prof. B.W. Ikua, Dr. J. N. Keraita and Dr. A. Niyibizi for their guidance, advice and support throughout my studies. Special acknowledgments also goes to all the members of staff of the Mechanical and Mechatronic Engineering Departments at Jomo Kenyatta University of Agriculture and Technology for their kindness and generosity especially in the use of facilities in the departments. I would also like to thank and acknowledge the Dedan Kimathi University of Technology in a very exceptional way for granting me the scholarship for my studies as well as a conducive environment with facilities. Last but not least, I thank and appreciate my family and friends for their prayers, care and support.

TABLE OF CONTENTS

LIST OF TABLES

LIST OF FIGURES

LIST OF ABBREVIATIONS

DOF	Depth Of Focus
CW	Continuous wave
FEA	Finite Element Analysis
FEM	Finite Element Method
HAZ	Heat Affected Zone
MEMS	Micro Electro Mechanical Systems
MOEMS	Micro Opto Electro Mechanical Systems
Nd:YAG	Neodymium: Yttrium Aluminium Garnet
TEM	Transverse Electromagnetic Mode

NOMENCLATURE

$\boldsymbol{A_l}$	Absorbtance (M^{-1})
$\boldsymbol{c_p}$	Specific heat at constant pressure (J/kg.K)
$\boldsymbol{C_c}$	Heat capacity of electron hole pairs (J/K)
$\boldsymbol{C_l}$	Heat capacity of lattice (J/K)
$\boldsymbol{C_L}$	Heat capacity of the liquid phase (J/K)
$\boldsymbol{d_{min}}$	Minimum beam diameter that can be achieved (M)
$\boldsymbol{D}$	Diameter of the unfocussed beam (M)
$\boldsymbol{E_g}$	Band-gap energy (J)
$\boldsymbol{E_m}$	The melting threshold energy (J)
$\boldsymbol{f}$	Lens focal length (M)
$\boldsymbol{h}$	Planks constant
$\boldsymbol{h_f}$	Heat of fusion (J/kg)
$\boldsymbol{h_g}$	Heat of vaporization (J/kg)
$\boldsymbol{K_b}$	Boltzmann's constant
$\boldsymbol{k_e}$	Thermal conductivity of the electrons (W/m.K)
$\boldsymbol{k_h}$	Thermal conductivity of the holes (W/m.K)
$\boldsymbol{k_l}$	Thermal conductivity of the lattice (W/m.K)
$\boldsymbol{K_L}$	Thermal conductivity of the liquid phase (W/m.K)
$\boldsymbol{m}$	Mass (kg)
$\boldsymbol{N}$	Density of state
$\boldsymbol{P}$	Laser power (W)
$\boldsymbol{Q}$	Heat generated per unit volume (W/m^3)
$\boldsymbol{R}$	Reflectance
$\boldsymbol{T}$	Transmittance

$\boldsymbol{T_b}$	Boiling temperature (K)
$\boldsymbol{T_c}$	Carrier temperature (K)
$\boldsymbol{T_e}$	Electron temperature (K)
$\boldsymbol{T_l}$	Lattice temperature (K)
$\boldsymbol{T_m}$	Melting temperature (K)
$\boldsymbol{t_p}$	Laser pulse duration (K)
$\boldsymbol{T_s}$	Temperature in solid state (K)
$\boldsymbol{u}$	Scanning velocity (mm/s)
$\boldsymbol{\alpha}$	One-photon absorbtion coefficient
$\boldsymbol{\beta}$	Two-photon absorbtion coefficient
$\boldsymbol{\sigma}$	Stress (N/M^2)
$\boldsymbol{\gamma}$	Auger recombination coefficient
$\hbar$	Reduced Planks constant
$\boldsymbol{\vartheta}$	Impact ionization coefficient
$\boldsymbol{\lambda}$	Wavelength (M)
$\boldsymbol{\rho}$	Mass density of the material (kg/m^3)
$\boldsymbol{\omega}$	Frequency
$\boldsymbol{\Omega}$	Collision frequency of particles

ABSTRACT

Monocrystalline silicon is an important material for the manufacture of MEMS and MOEMS devices. Formation of microcracks and extensive heat affected zones are major challenges associated with laser micromachining. In recent times, lasers have gained popularity in micromachining applications. This trend has been due to the various unique properties that lasers possess. These properties include the ease of manipulation, and the ability to focus the beam to a small spot.

In this research, effects of the Nd:YAG laser beam and process parameters on cut quality attributes of monocrystalline silicon were investigated. The parameters investigated were: scan speed, power and beam spot diameter. The quality attributes investigated were kerf depth, and thermal stress effects such as microcracks formation. A numerical model was developed using finite element analysis method to investigate the parameters and attributes.

The results of the study show that increasing the laser scan speed led to a decrease in the kerf depth and a decrease in microcracks formation. Also, increasing the spot diameter of the beam led to a decrease in kerf depth and a decrease in the microcracks formation. Increasing the laser power led to an increase in kerf depth, and an increase in microcracks formation. The simulation results were validated by comparison to experimental ones. The models satisfactorily predicted the expected kerf depth and microcrack formation for the laser parameters studied.

CHAPTER ONE

1.0 INTRODUCTION

1.1 Background

There are few traditional techniques available for the precision machining of silicon. These include scribing, grinding, lapping and saw dicing. Unfortunately, this methods have certain drawbacks in that they cause undesired scratches and chipping of the cut edge [1, 2]. The surface generated therefore requires further machining and cleaning to improve the quality of the finish. In addition, the force exerted by the cutting tool produces microcracks in the material and the subsequent breaking step yields small chips and debris [2]. Furthermore, mechanical cutting leaves significant residual stress in the finished component [1]. This residual stress may cause cracking of the monocrystalline silicon while in operation reducing thus its reliability.

Lasers have been used successfully in machining of hard and brittle materials [3].Research performed so far shows that laser machining of monocrystalline silicon may overcome several of the limitations encountered with traditional methods. Laser machining offers new possibilities for processing monocrystalline silicon since it does not require any mechanical cutting force and does not result in any form of tool wear [3]. During laser micromachining, material separation is achieved by scribing, melting, vaporization or thermal fracture [3]. Vaporization and melting modes are energy intensive techniques demanding high values of power density.

Monocrystalline silicon has been subjected to experimental and theoretical research in recent years [4]. The highly perfect crystalline structure of pure silicon single crystals is usually the starting point for many electronic applications [5]. Laser micromachining of monocrystalline silicon is currently applied in the manufacture of different Micro Electro-Mechanical Systems (MEMS) and Micro Opto-Electro Mechanical Systems (MOEMS). Micromechanical components as acceleration sensors in car safety systems and micro-fluidic circuits are made of silicon. Silicon is also used as a substrate for X-ray mirrors. [6].

During the laser micromachining of monocrystalline silicon, microcracks of varying sizes result due to thermal stresses [7]. The microcrack sizes depend on the laser source being used and the laser process parameters. These microcracks contribute to irregularities in the machined silicon.

Monocrystalline silicon is usually distorted during Nd:YAG laser micromachining due to the extensive heating and thermal stresses. Selection of the optimal laser beam and process parameters can significantly affect the cut quality attributes of monocrystalline silicon microdevices. Numerical investigation on the influence of the laser scan speed, laser power and laser beam spot size on cut quality attributes such as kerf depth and microcrack formation will form the basis of this research.

1.2 Problem statement

Monocrystalline silicon is hard and difficult to machine and is usually distorted during Nd:YAG laser micromachining. Excessive laser heat input may lead to extensive heat affected zones and resulting thermal stresses. The thermal stresses in the material enhance microcrack formation. Microcrack presence in monocrystalline silicon microdevices lowers its strength, which may eventually lead to the failure of the final components [8].

In recent years, greater emphasis has been placed on laser micromachining of miniaturized silicon microdevices. Their application calls for high accuracy and surface quality. For example, in the case of medical microfluidic devices, the cut quality of microchannels affects the flow, mixing and delivery of drugs. There is need to develop computational methodologies for studying the influence of laser machining parameters on the cut quality attributes such as kerf depth and microcracks. This research work will study the laser machining parameters such as beam spot size and laser process parameters such as scan speed and power. The relationship between the various laser machining parameters and the output attributes need to be established so that they can be controlled during laser micromachining of monocrystalline silicon to attain desirable outcomes.

1.3 Objectives

To develop a mathematical model relating laser machining parameters and induced thermal stresses and to optimize these parameters for quality laser micromachining of monocrystalline silicon.

The specific objectives are:

- To develop a mathematical model for predicting the optimal laser beam and laser process parameters for quality micromachining of monocrystalline silicon.
- To determine the optimal laser machining parameters for desired quality attributes in micromachining of monocrystalline silicon.
- To validate the developed model.

1.4 Justification

This research will help in understanding how the various laser beam process parameters in laser micromachining of monocrystalline silicon affects the vital performance attributes such as surface quality and dimensional accuracy. The results of the study can guide the laser operator in selecting the optimum laser machining parameters for attaining the desired outcome. The results of this research may also be used as a baseline for further research into laser micromachining and can be extended to other materials.

1.5 Thesis Outline

The thesis contains seven chapters. The present chapter provides a background on the laser micromachining of monocrystalline silicon. It also highlights the existing problems and objectives of the study. Chapter TWO presents a critical review of the available literature on the basic principles of laser and describes the various material and laser parameters. Developments in laser machining and modeling are presented here. Challenges of previous numerical models are also highlighted. Presented in chapter THREE is the mathematical formulations for the laser micromachining process. The heat equation and crack propagation equations are described. The laser material interaction process is also presented. In Chapter FOUR, the numerical solution of the equations of the mathematical model is presented. The Finite Element Method and Galerkin approach for solving the discretized equations are presented. The system assembly and boundary conditions are also described. Chapter FIVE discusses the results from the study. The results of the effect of laser scan speed, spot size and power on the temperature distribution and thermal stresses are presented, the resulting laser micromachining attributes are discussed. These attributes are kerf depth and microcrack formation. The results are validated by comparison to existing experimental ones. Chapter SIX gives the conclusions of the main findings. The areas requiring further research effort on the subject are presented in chapter SEVEN.

CHAPTER TWO

2.0 LITERATURE REVIEW

2.1 Overview

A lot of research has also been carried out to study the effects of the various laser beam parameters on the quality of the cut as well as surface finish of a product [3]. Since each material responds differently to laser irradiation, the beam and process parameters have to be adjusted accordingly to attain the most favourable machining performance. Several experimental studies to investigate the basic laser machining processes have been carried out over the last few years [9].

The determination of efficient laser beam and process parameters for the micromachining of silicon is a major challenge for the solar cells manufacturing industry and microfluidic device manufacture. In an effort to overcome this challenge, the role of the laser pulse duration, wavelength, size of the laser spot, pulse repetition rate, laser beam incidence angle, initial temperature of silicon crystals, thermal conductivity and brightness of silicon have been studied performed to provide a more complete picture of the laser micromachining process [10]. Initially the basic principles of laser generation are explored.

2.2 Basic principles of lasers

A laser is an optical oscillator consisting of two reflectors placed parallel to each other where light bounces back and forth between the reflectors indefinitely unless stopped by a mechanism such as absorption, scattering or diffraction. Between the mirrors is an active medium capable of amplifying the light oscillations by stimulated emission, the process after which the laser was named: Light Amplification by Stimulated Emission of Radiation [3].

The stimulation phenomenon was predicted by Albert Einstein in 1916 [11]. He hypothesized that if a molecule or an atom is in an excited state, it will give up its energy if acted upon by a quantum of the same energy. Figure 2.1 shows a typical laser system setup [11]. An excitation or pumping source is required so that the lasing medium has the energy to become active and is usually dependent on the type of laser in question.

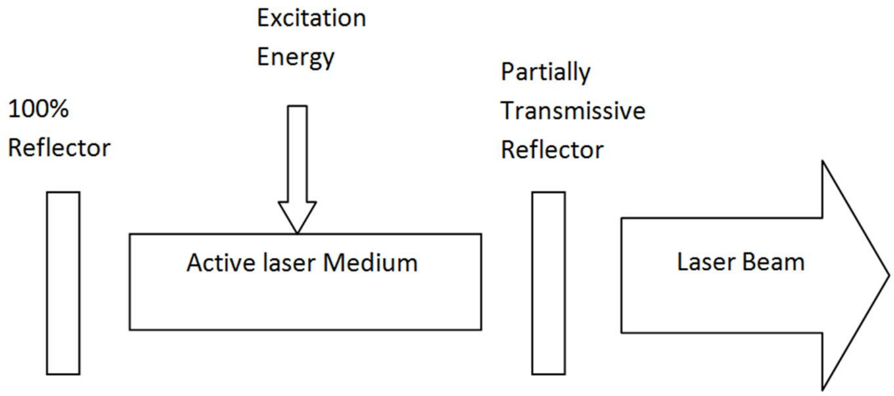

Figure 2.1: A typical laser system.

Initially, the excited atoms or molecules of the active medium fall back to their natural un-excited state emitting the excitation energy in form of packets of light energy called photons in what is known as spontaneous emission [11]. Only the photons emitted parallel to the optical axis formed by the two reflectors eventually survive as the other photons are lost through the mechanisms such as absorption by the optical cavity's walls [11].

In the process of traveling to and from reflectors, atoms collide with each other and as predicted by Einstein, the excited atoms are stimulated to give off their energy. This process repeats itself many times as the excitation source is still pumping atoms to a higher energy state and the photons parallel to the optical axis keep multiplying hence the amplification. The stimulated photon has the exact characteristics of the atom that stimulated its emission including the direction of travel. If one of the reflectors is partially transparent, then a beam of significant power emerges. The other reflector is made totally reflective to facilitate the amplification process and is usually curved to reduce diffraction losses of the oscillating energy as well as ease the alignment process [11].

The length of the optical cavity in which the lasing process takes place is usually larger than the width and it is considered that the field of the waves traveling inside the cavity is split into transverse and longitudinal modes that are nearly independent of each other [12].

2.3 Laser parameters

The laser transverse electromagnetic mode (TEM) describes variation in beam intensity with position on a plane perpendicular to the beam propagation direction [12]. The patterns on Figure 2.2 represent the various mode patterns showing how the laser beam is distributed on the transverse section [12]. These patterns are the transverse electromagnetic modes, TEM_{mn}, where the subscripts m and n represent the number of nulls in the two directions perpendicular to the laser's optical axis. Nulls are the regions where the laser light is not bright. The TEM_{00} mode has no nulls in either of the mutually orthogonal transverse directions.

The mode pattern affects the distribution of the beam output energy hence affecting the machining process and the machining outcome. The more split up the beam is on the transverse section, the higher the order of the beam. It is harder to focus a higher

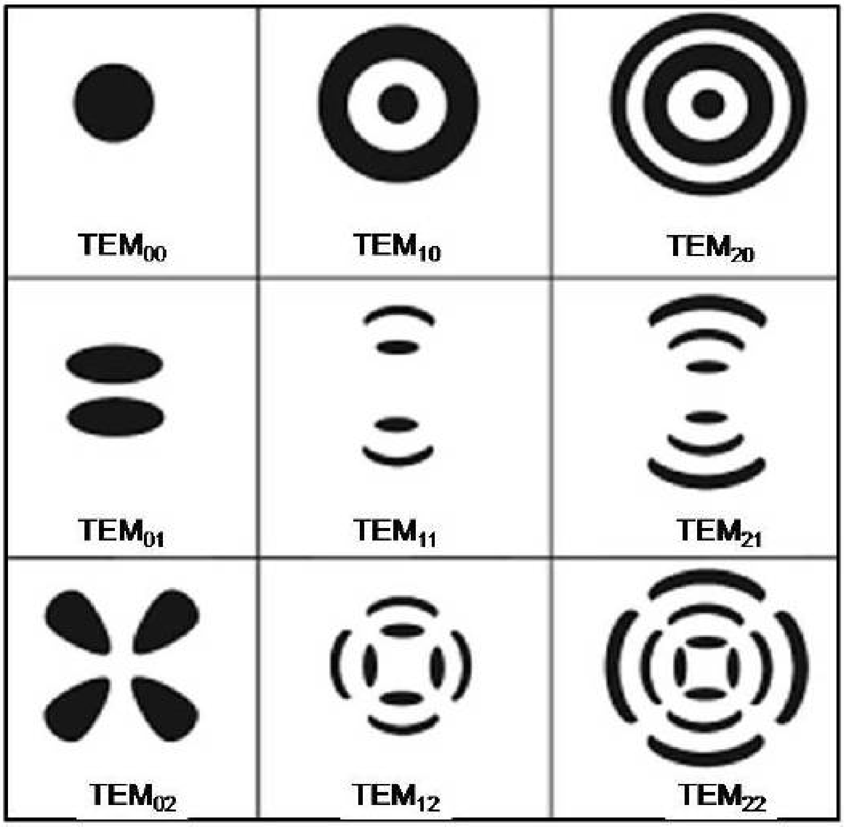

Figure 2.2: TEM patterns

order of the beam than lower orders because the higher order is not from a virtual point but is from patterns [12].

The longitudinal modes which are field configurations along the optical axis determine the frequencies the laser operates in. In the direction normal to the laser axis, the field inside the cavity often consists of transverse configurations that propagate back and forth along the laser axis. The pattern of the transverse field configuration does not change after completion of the longitudinal round-trip between the two reflectors [12].

These patterns are the ones commonly encountered in many practical lasers [13]. The lowest-order transverse mode, for which $m = n = 0$, is commonly called the fundamental mode. This is because the field distribution is described by a Gaussian function. This kind of beam is called the Gaussian beam. Operation in the Gaussian mode is desirable because of the simple spatial profile and the lack of nulls in the distribution of the intensity across the beam, making the focusing of the beam easier. The spatial profile of the Gaussian beam will retain its Gaussian form as the beam propagates and is transmitted through optical systems. Other higher-order modes will not retain their original spatial distribution as the beam propagates [12].

TEM_{00} has the highest quality, with a beam propagation factor $M^2 = 1$ and gives the smallest and sharpest spot size. It also has the lowest divergence and gives the highest power density. The quality falls with higher orders for the same power and spot size of the beam at the focusing lens. TEM_{01} for example, has a beam propagation factor $M^2 = 1.7$ with a larger spot size which will produce a wider kerf width during machining [12].

The wavelength(λ) of the laser is determined by the corresponding stimulated energy transition. When interacting with materials, different wavelengths will cause different effects. Shorter wavelengths have higher energy in the photons. The laser wavelength also has influence on the maximum resolution and the focal properties. Shorter wavelengths produce higher resolutions and better focal properties [14].

Laser power is the optical output power of the laser. The output power has influence on the process time and cost of operation. Lower laser power leads to longer processing time as higher laser power leads to higher operating costs [14].

The focal spot size of the laser is an important parameter in material processing because it determines the power intensity and maximum energy density that a given laser beam can deliver. When a beam with a finite diameter D is focused by a lens onto a plane, individual rays of the beam striking the lens can be considered as point radiators of new wave front. The rays passing through the lens are converged onto the focal plane with constructive and destructive superposition taking place [14]. Figure 2.3

shows the profile of the power intensity. The focal diameter is measured at the point

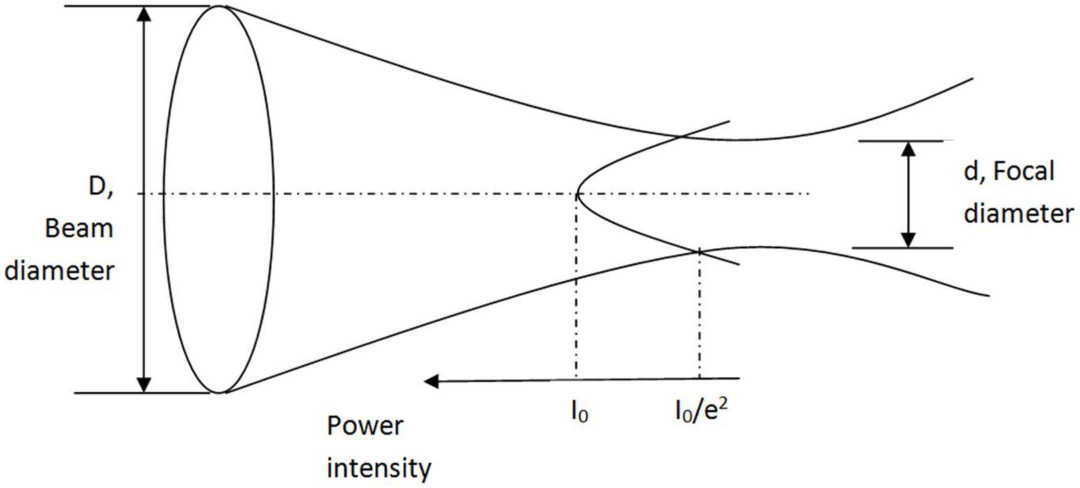

Figure 2.3: Gaussian power distribution at the focal point.

where the intensity is $\frac{1}{e^2}$ of the peak value. e is the exponential of the curve. For a parallel rectangular beam with a plane wavefront, the diffraction limited minimum beam diameter is given by Equation 2.1.

$$d_{min} = \frac{\lambda f}{D} \tag{2.1}$$

Where f is the lens focal length, λ is the laser wavelength and D is the diameter of the unfocussed beam. If the beam is circular, the equation becomes [14].

$$d_{min} = \frac{2.44\lambda f}{D} \tag{2.2}$$

If the beam is a multi-mode beam TEM_{01}, the minimum beam diameter is obtained by Equation 2.3.

$$d_{min} = \frac{2.44\lambda(m+n+1)f}{D} \tag{2.3}$$

Where m and n represent the order of the laser mode [14].

The depth of focus (DOF) is the distance about the focus over which the laser beam has approximately the same intensity as shown in Figure 2.4.

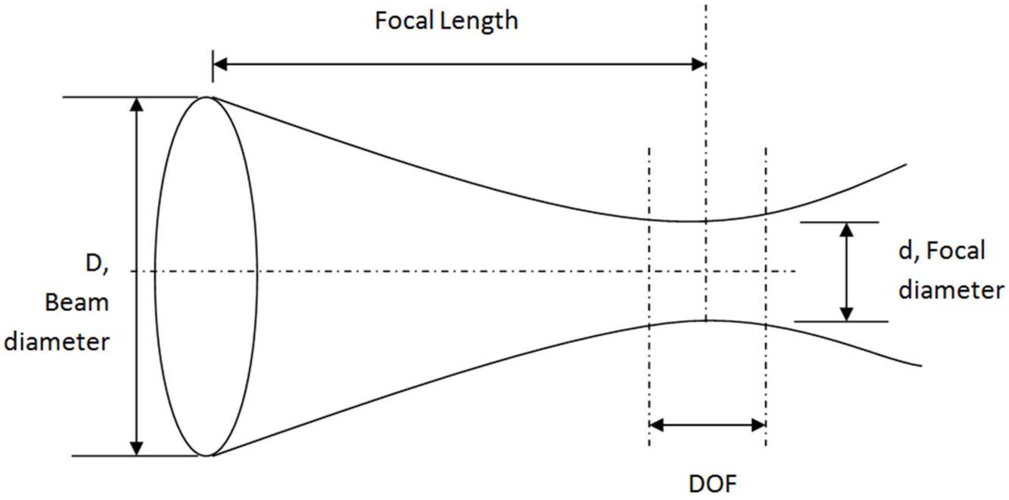

Figure 2.4: Depth of focus of a laser beam.

The DOF is the distance within which the focal spot size changes by -5 percent to 5 percent. Equation 2.4 is the expression for obtaining the depth of focus [14].

$$DOF = (\frac{8\lambda}{\pi})(\frac{f}{D})^2 = 2.44(\frac{f}{D})^2 \tag{2.4}$$

A longer depth of focus is desirable for through thickness processing to provide approximately equal energy density along the material thickness [15]. The length of the DOF also has influence on the formation of tapered edges during laser machining.

2.4 Material parameters

The interaction between the beam and the material starts with the relationship between absorptance, reflectance and thermal conductivity shown in Equation 2.5.

$$A = 1 - R - T \tag{2.5}$$

Where A is the absorptance, which is variable with the wavelength of the laser for a specific material. High absorptance of a certain wavelength by a material increases its machinability with a laser of that wavelength. R is the reflectance, which is a ratio of reflected laser power to the power incident on the material. T is the thermal conductivity of the material with higher conductivity requiring more energy for machining [16].

The thermal expansion coefficient of a material is also a significant parameter for silicon, as it leads to crack formation in materials with low thermal conductivity, as a result of high thermal gradients that cause high mechanical stresses [17].

2.5 Developments in laser machining

2.5.1 Laser Beam Machining

Laser beam machining is a thermal material removal process which makes use of a high energy, coherent beam of light to melt or vaporize particles on the surface of a workpiece. A schematic illustration of the laser beam machining method is shown on Figure 2.5. The laser beam used for machining may be operated in continuous wave (CW) mode or pulsed beam mode as shown on Figure 2.6 [18]. CW operation has the advantage of smooth surface after machining. Pulsed beam operation allows for deeper drilling or cutting depth to be achieved compared to a continuous beam operating at the same beam power.

The laser machining process may be classified into one-dimensional, two-dimensional or three-dimensional process as illustrated by Figure 2.7. The laser beam being a directional heat source, can be viewed as a one dimensional line source with a line

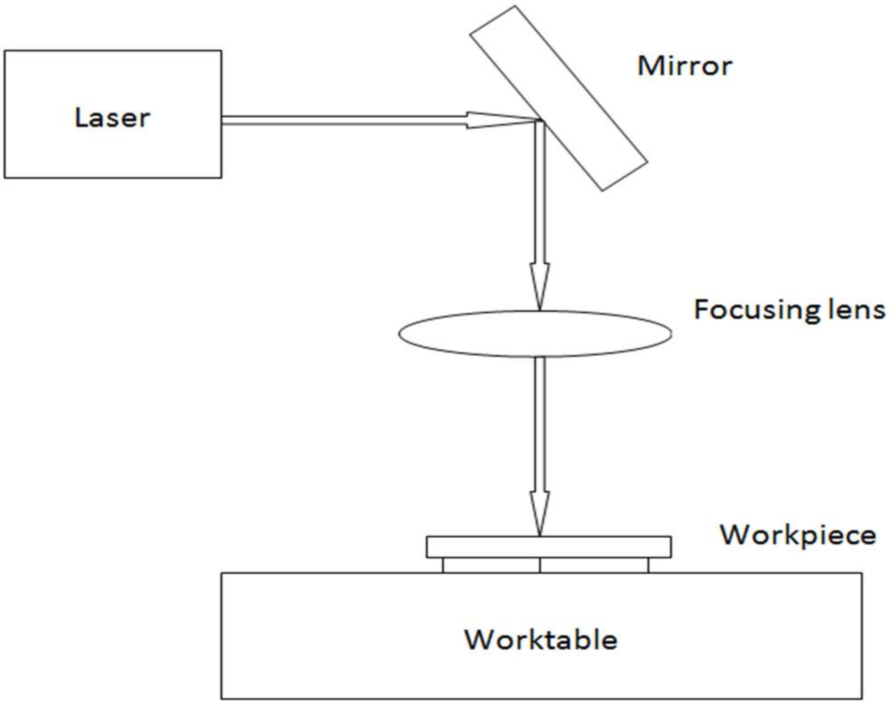

Figure 2.5: Laser beam machining.

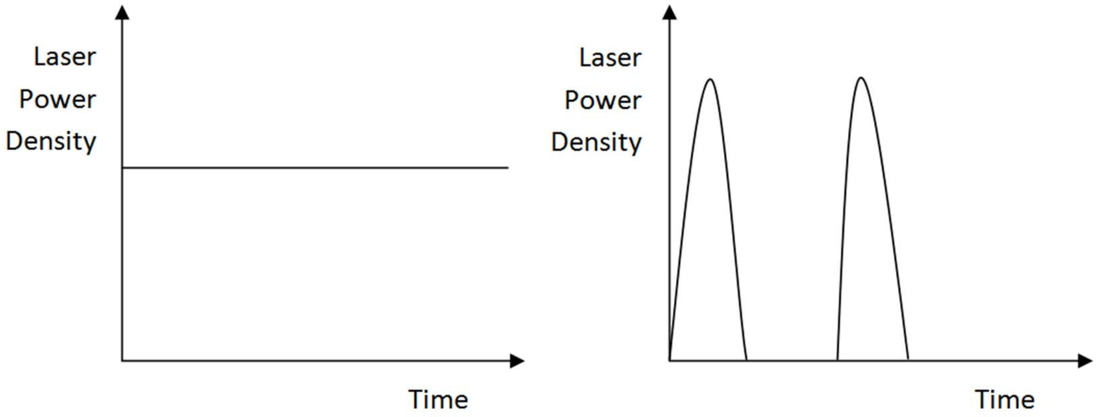

(a) Continuous wave

(b) Pulsed Mode

Figure 2.6: Laser beam temporal modes.

thickness equal to the beam diameter [18].

For a one dimensional process such as drilling, the laser beam is stationary relative to the workpiece as shown on Figure 2.7(a). The erosion front,which is located at

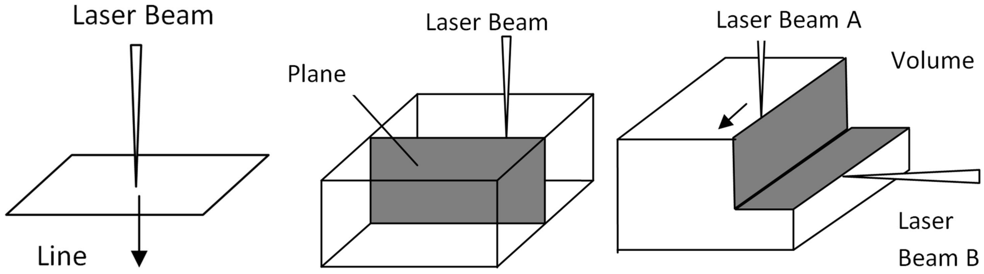

(a) One-dimensional laser machining (Drilling) (b) Two-dimensional laser machining (Cutting) (c) Three-dimensional laser machining (Milling)

Figure 2.7: Classification of laser machining based on erosion fronts.

the depth of the drilled hole, propagates in the direction of the line source in order to remove the material. In case of two dimensional process such as cutting shown on Figure 2.7(b), the laser beam is in motion relative to the workpiece. Material removal occurs by moving the laser source in a direction perpendicular to the laser direction forming a two dimensional surface. The erosion front is located at the leading edge of the line source.

For three dimensional machining such as milling, two or more laser beams are used and each beam forms a surface through motion relative to the workpiece as shown on Figure 2.7(c). The erosion front for each surface is found at the leading edge of each laser beam. Where the cut surfaces intersect, the three dimensional volume bounded by the surfaces is removed.

The two most commonly used industrial application lasers are the CO_2 laser that operates at a wavelength of $10.6\mu m$ and the Nd:YAG laser whose wavelength is $1.06\mu m$. Some common industrial laser applications include cutting, welding and micromachining and are listed in Table 2.1 [19, 20]. The output of the laser can be continuous, constant amplitude, known as continuous wave (CW) mode, or periodic, known as pulsed beam mode. In continuous beam operation, constant laser energy is discharged

Table 2.1: Common Industrial Laser Applications

Type	**Operating Mode**	**Maximum Power (Watts)**	**Applications** .
CO_2	Pulsed	3000	Cutting, welding, drilling, marking
CO_2	Superpulsed	5000	Cutting .
CO_2	Continuous	25000	Cutting, welding, surface treatment
Nd:YAG	Pulsed	2000	Cutting, welding, drilling, marking, micro-machining
Nd:YAG	Continuous Wave	3000	Cutting, welding, surface treatment
Nd:YAG	Q-Switched	150	Drilling, marking, micro-machining

uninterruptedly for a relatively long time. In pulsed mode of operation, the pumped energy is stored until a threshold is reached. Once the threshold is reached, the stored energy is rapidly discharged into short duration pulses of high energy density [21].

The CO_2 laser is a gas laser that emits light in the infrared region and is capable of producing power up to 25KW in continuous wave mode and up to 1MW in pulsed mode. The Nd:YAG is a solid state laser which can deliver machining energy through a fibre optic cable. It is capable of producing up to 1KW in continuous mode and up to 50KW in pulsed mode [21].

The lasers system used for micromachining employ normally pulsed beams with an average power of well below 1 kW while those used for macro machining use generally CW laser beams ranging up to several KW. CW lasers produce constant power. This property presents challenges during micromachining. CW lasers causes extensive heat affected zones as a result of uncontrolled heat input into the material [21].

The field of micro-machining includes manufacturing methods like drilling, cutting, welding as well as ablation and material surface texturing, whereby it is possible to achieve very fine surface structures ranging in the micrometer domain [3]. Such processes require a rapid heating, melting and evaporation of the material. The use of extremely short nanosecond pulse durations helps to minimize the thermal effects such as melting and thermal stress effects such as microcrack formation, thus eliminating the need for any post processing measures such as etching [3].

Monocrystalline silicon absorbs light well in the range of 1064 nm. Nd:YAG laser operates at a frequency of 1064 nm, thus making it the best choice for micromachining of monocrystalline silicon. CO_2 laser has a wavelength of 10640 nm, thus the light would be poorly absorbed by the monocrystalline silicon [3].

2.5.2 Laser micromachining with a dual focused laser beam

One way to generate two focal spots from a single laser source is to use a dual-focus lens. Figure 2.8 shows the schematics of the setup for the dual focus laser micromachining [22]. Dual focus can be used for all laser ablation processes such as cutting, drilling and scribing to improve the machining efficiency and the cut quality [22]. This techniques presents a challenge because the dual focus lens is not suitable for monocrystalline silicon micromachining due to the long separation distance between the two focal points (separation in the range of tens or hundreds of microns) [19].

2.5.3 Water jet guided laser micromachining of silicon

Figure 2.9 shows a schematic illustration of the principle of the water jet guided laser micromachining. Water jet guided laser technology entails coupling of a high power pulsed laser beam into a hair thin, low-pressure water jet [23].

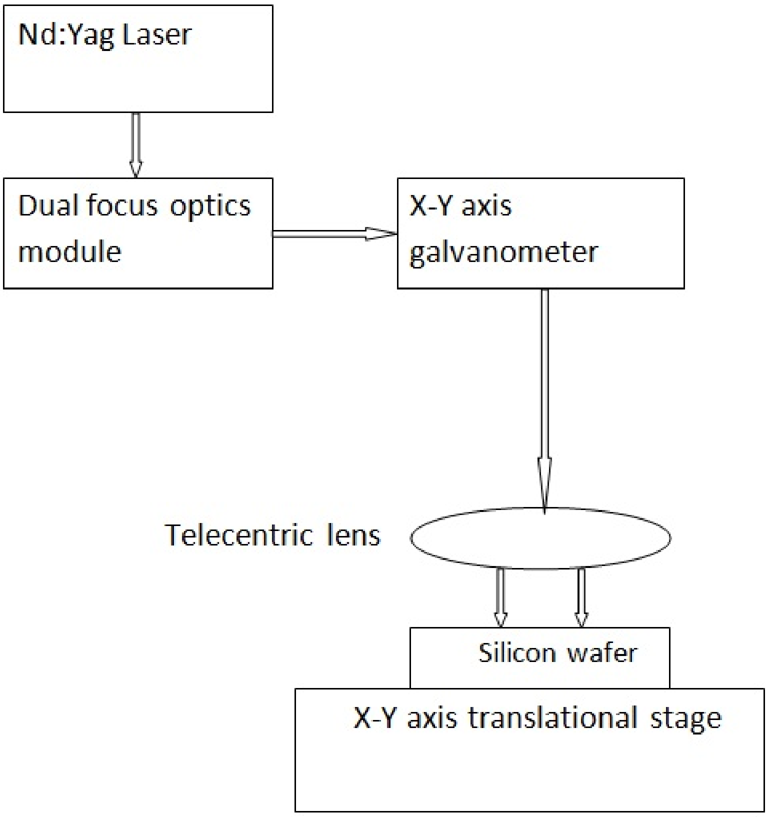

Figure 2.8: Illustration of dual focus dicing setup.

Conventional dry laser micromachining process presents some challenges. First, since the laser beam is focused, this causes the resulting micromachined kerf to taper. Water jet micromachining overcomes this challenge since the water jet cylindrical shape provides a parallel guide to the laser beam. The resulting micromachined kerf walls are highly parallel. Secondly, conventional dry machining results in extensive heat affected zone. Water jet machining overcomes this challenge by using the pressurized water to remove heat from the workpieces. Thirdly, after dry laser cutting process, molten silicon resolidifies inside the kerf walls and hence distorts kerf profiles. This challenge can be overcome by the water pressure feature of the water jet machining.The water jet develops a high kinetic energy which removes molten silicon and hence ensure minimal molten silicon resolidification. [24].

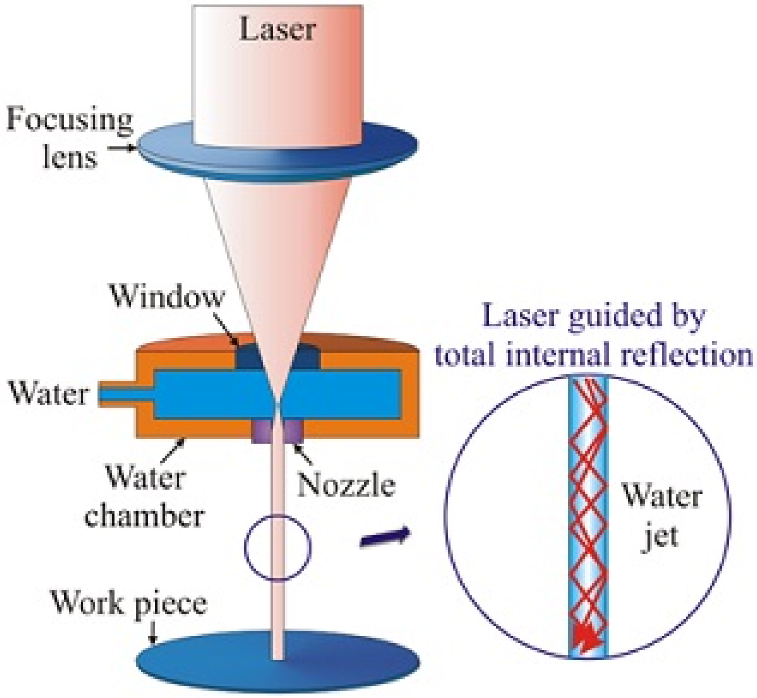

Figure 2.9: Basic principle of the water jet-guided laser technology.

2.6 Laser beam delivery system

Harnessing the power of a high-power laser requires knowledgeable and prudent choices made when selecting the laser and its beam delivery system. Boyd [25] investigated the operation of the optical fiber and provided some guidelines for specifying a system. He found that fiber length was a factor, as light of some initial distribution propagates in the fiber, it was either converted into modes supported by the fiber, or it was lost and appeared as leakage or heat. This conversion, however, required a certain length of fiber to be affected and different length scales had to be considered: short, intermediate and long.

His works revealed that smaller fibers produced less degradation to beam quality, but the spot size of the beam focused into the fiber was limited by the quality of the laser beam, focusing optics and the numerical aperture of the fiber. Bends in the fiber-optic cable produced higher order modes that modified the beam profile. Consequently, a length of rigid sheathing for the output end of the fiber maintained the beam quality and improved resistance to handling effects [25].

2.7 Modeling of laser cutting of silicon

Two major numerical techniques used for laser modeling are Finite Difference Method (FDM) and Finite Element Method (FEM). Several researchers have used FDM to analyze laser machining. Kar et al. [26] developed a two-dimensional model for material damage during laser melting and vaporization using the Crank-Nicholson method where finite difference method was used to numerically solve the heat equation [27]. The effect of curvature of solid-liquid and liquid-vapor interfaces, laser power, time, number of pulses, and laser beam diameter on depth and radius of the crater during laser irradiation were taken into account. The linear relationship between the maximum crater depth and the laser intensity was derived phenomenologically and verified numerically. It was observed that the maximum achievable crater depth increased with increasing laser intensity. However, the model did not consider a moving laser machining scenario.

Cheng et al. [28] developed a steady state, two dimensional finite difference mathematical model to simulate heat flow and material removal by volatilization. Voisey et al. [29] used the model developed by Cheng to predict hole profile and thermal fields in laser drilling. The two latter models could not solve for hole profiles and thermal fields for three dimension material.

Mazumder et al. [30] developed a three dimensional model of laser materials processing with a moving Gaussian heat source using finite difference numerical technique. This model was used to predict temperature profile, maximum processing speed and heat affected zone in the region of laser-surface interaction. Modest [31] put forward a three-dimensional transient ablation model for laser machining ceramics to predict transient temperature distribution and groove shape. Finite difference method was used to solve the three dimensional conduction equation. The FDM model was not suitable for solving thermal stresses developed within the material. Thermal stress is an important factor to consider in modeling of hard and brittle materials.

Finite element models are widely used for calculating stress, strain, strain-rate and temperature distribution in the cutting zones. Treatment of laser processing using finite element was demonstrated by Yu [32] who developed a model which incorporated boundary and loading conditions, as well as phase changes in the laser cutting process. However, this model could not predict thermal stresses developed within the material. Yu used the $ANSYS^R$ Parametric Design Language and showed that the numerical method compared well with experimentally obtained results [33].

Bianco et al. [34] proposed two numerical models for two and three dimensional models to evaluate transient and conductive fields due to moving laser sources. The analysis was extended to a semi-infinite solid through a transient numerical model given in [35]. A three dimensional transient conductive model was also developed using $COMSOL^R$ 3.3 code [36]. A Gaussian laser source was considered moving with constant scan speed along the cutting direction. Thermal properties were assumed to be temperature dependent and surface heat losses toward the ambient were taken into account on the external transversal surface of the solid. Temperature profiles and fields showed that a quasi steady state was reached. This model however, failed to consider the effect of convective heat transfer on the transversal surface of the semi-infinite solid.

In some previous studies, Meung [37] considered a three-dimensional computational model of evaporative laser-cutting process developed using a finite element method. Steady heat transfer equation was used to model the laser-cutting process with a moving laser and assumed a continuous wave Gaussian beam [38]. The finite element surfaces on evaporation side were non planar and were approximated by bilinear polynomial surfaces [39]. Semi-infinite elements were introduced to approximate the semi-infinite domain [38]. An iterative scheme was used to handle the geometric nonlinearity due to the unknown groove shape. The convergence studies were performed for various meshes. The finite element model, however, failed to consider the influence of convection and surface reflection, energy loss due to the erosion front and resolidified decomposed material.

Liu [40] conducted a numerical study on thermal stress cutting of silicon wafer using a two-point pulsed laser. In his work, Nd:YAG laser cutting using the controlled fracture technique showed great potential to be used for the separation of brittle materials. In this technique, thermal stress was used to induce the crack and the material was separated along the moving direction by extending the crack. The mechanism of crack propagation, the effects of laser power and the distance between the two spots on the development of thermal stresses were investigated. The numerical results revealed that thermal stress was affected by laser power and the distance between the two laser spots. This numerical study, however, failed to consider the influence of various scan speeds and beam spot sizes on the thermal stress.

The von Mises yield criterion, usually applied to metallic materials, has been applied to brittle materials such as silicon and concrete. Brock [41] utilized von Mises criterion in thermoelastic problem to define fracture for brittle materials. His work investigated the fracture initiation in multilayered thin film systems.

2.8 Summary

From the foregoing review, there has been a lot of work done in developing models to predict the quality of laser micromachining of silicon and that considerable progress has been made. A mathematical model that helps predict kerf depths and thermal-stress effects shall play a significant role in laser micromachining of monocrystalline silicon.

Different modeling methods have been used in the modeling of silicon behaviour during laser micromachining. This techniques have encountered several challenges. The Finite difference methods have been used by several researchers for two dimensional modeling. These models, however, were not suitable for solving thermal stresses developed within the material. Thermal stress is an important factor to consider in modeling of hard and brittle materials behaviour during silicon laser micromachining.

Finite difference methods have been used by several researchers for two and three dimensional modeling. These models, however, could not successfully predict temperature distribution within the material. The models failed to include the effect of convective heat transfer and surface reflection of the material. The models did not highlight the influence of various scan speeds and beam spot sizes on the thermal stress developed. Existing research has not satisfactorily explored the influence of laser scan speeds, power and beam spot sizes on output attributes such as kerf depths and microcrack formation.

This present work aimed to provide a model for laser cutting, taking into account the effect of laser light absorption within the silicon, temperature changes and stress within the silicon. This will improve on previous models and lead to a better understanding of microcrack formation in silicon, specifically monocrystalline silicon.

The model will also help to evaluate the influence of the laser processing parameters such as scan speed, power and spot size, and how they can improve the cut quality attributes of monocrystalline silicon. This model will help reduce the cost involved in mounting experiments. It will also help bring out process information relating to conditions for improved accuracy and predictability in a cost effective way.

CHAPTER THREE

3.0 MATHEMATICAL FORMULATION FOR THE LASER MICROMACHINING PROCESS

3.1 Background

This chapter discusses the mathematical model used to simulate the process. In general, for complex beam profiles, the wave equation for the entire spatial intensity distribution of the light within the material is solved first, then the magnitude of the gradient of intensity is taken as the volumetric heating rate due to laser absorption as input into the heat equation.

3.2 Modeling and simulation - Simplifying assumptions

The thermal model which is described by the temperature field in the work piece has to be determined as a necessary first step in the laser cutting simulation. The solution will be uniquely defined provided that appropriate initial and boundary conditions are given. The major assumptions on which the model is based are as follows:

1. Thermophysical properties are constant and uniform.
2. The laser beam has a Gaussian distribution in pulsed mode.
3. The Fracture stress is $300 \times 10^6 Pa$
4. The material is assumed to be isotropic, homogeneous and linear elastic.

A finite element model is established based on $COMSOL^R$ [36]. The coarse finite meshes of the model are shown in Figure 3.1. A cutting line is formed by using a parametric curve to generate a straight path across the work piece. The mesh is then altered to a finer mesh along the laser path to improve the accuracy of the results. A simulation test is performed under constant conditions for all the four element sizes. The results are as shown in Figure 3.2. The images show the comparison of how mesh size selection can affect quality/resolution of the results. Figure 3.1 shows the various mesh size choices for the domain of the material.

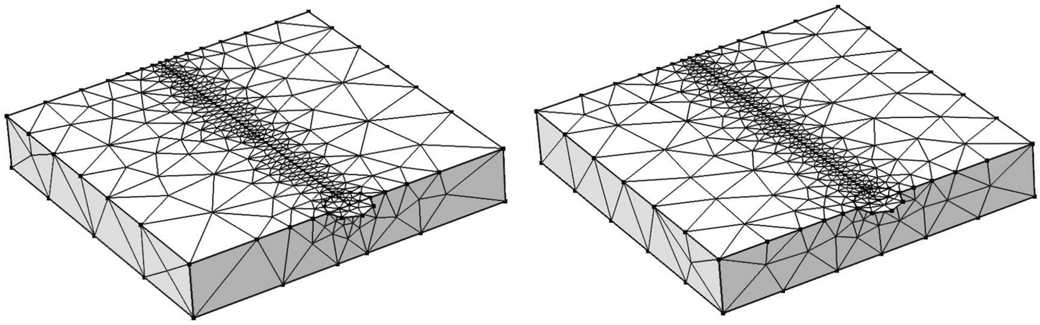

(a) Very coarse mesh (b) Coarse mesh

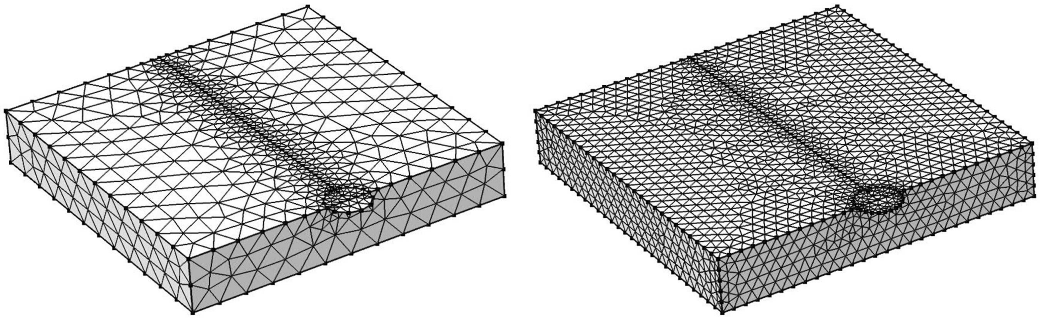

(c) Fine mesh (d) Very fine mesh

Figure 3.1: Various mesh sizes for the domain of the material compared with the resulting effects.

The very coarse mesh (Figure 3.1a), had 760 elements and its computational time was 50 minutes. The coarse mesh had 2030 elements (Figure 3.1b) and its computational time was 2 hours. The fine mesh had 6322 elements (Figure 3.1c) and its took 5 hours to solve for the results. The very fine mesh had 19764 elements (Figure 3.1d) and its computational time was 16 hours. A very fine mesh consumes computational time than all the other meshes. This is because the solver for the simulation software has to perform calculations for each element before proceeding to the next element. judging from these observations, the optimal mesh size was found to be the fine mesh.

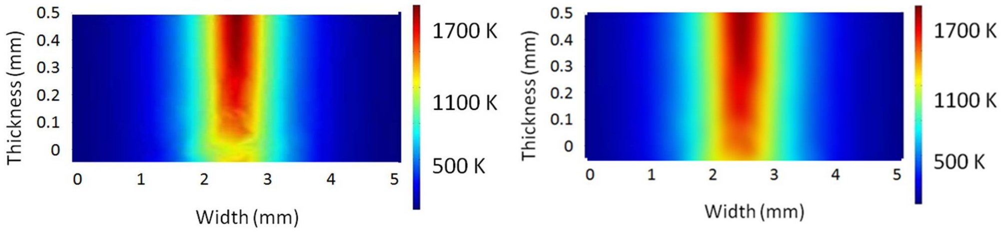

(a) Very coarse mesh

(b) Coarse mesh

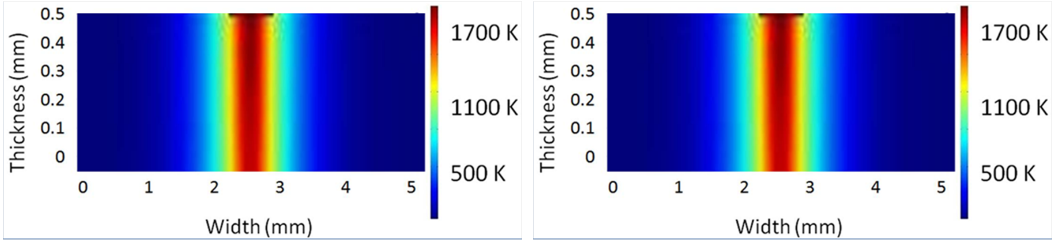

(c) Fine mesh

(d) Very fine mesh

Figure 3.2: Temperature distribution results obtained from various mesh sizes.

Figure 3.2 shows the resolution of temperature distribution results obtained from various mesh sizes. The resolution of the results obtained when using the very coarse mesh are shown in Figure 3.2a. The resolution of the results obtained when using the coarse mesh are shown in Figure 3.2b. For these two latter mesh sizes, the resolution is poor. Hence, this will affect the accuracy of results. The resolution of the results obtained when using the fine mesh are shown in Figure 3.2c. The resolution of the results obtained when using the very fine mesh are shown in Figure 3.2d. For these two latter mesh sizes, the resolution is good. Hence, the accuracy of results for this element sizes is good. A fine mesh for the entire model can also be used to obtain good accuracy on all the points of the model. However, it would greatly increase the computational time.

The finite element solution to these equations can be obtained by divide the solid body into several tetrahedron elements. A tetrahedral element was selected for this computation. Figure 3.3 shows a single cell for the tetrahedral element. i, j, k and l are nodes for the element with coordinates in the X, Y, Z cartesian coordinate system. The choice of tetrahedral mesh over hexahedral mesh for 3 dimensional domain is because the hexahedral mesh generation takes several orders of magnitude longer than current tetrahedral mesh generators to complete.

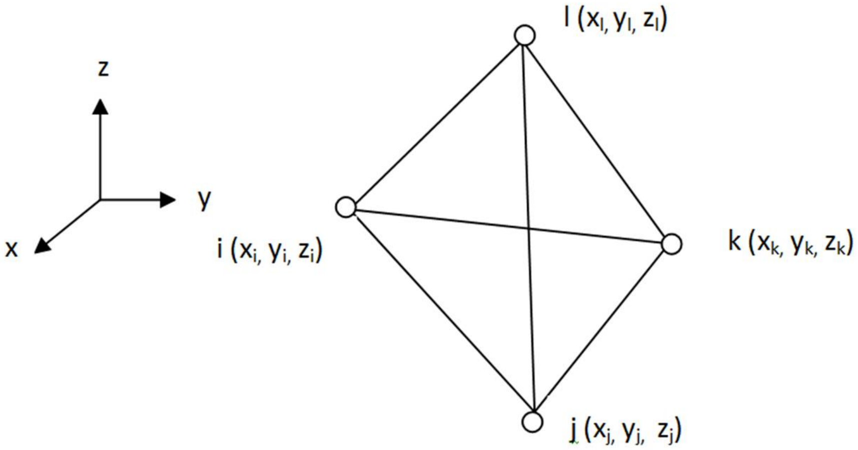

Figure 3.3: A tetrahedral element.

3.3 The Heat equation

The heat equation is derived from the conservation of energy and Fourier's law of heat conduction, which states that the local heat flux is proportional to the negative of the gradient of the temperature [42]. In a coordinate system that is fixed with the laser beam, the heat equation in one dimension can be written as:

$$\begin{aligned}\rho(x,T)c_p(x,T)\frac{\partial T(x,T)}{\partial t} &- \nabla[k(x,T)\nabla T(x,T)] \\ +\rho(x,T)c_p(x,T)\upsilon_s\nabla T(x,T) &= Q(x,T)\end{aligned} \tag{3.1}$$

where ρ is the mass density of the material, c_p is the specific heat at constant pressure, k is the thermal conductivity and v_s is the velocity of the substrate relative to the heat source. The left hand side of this heat equation describes the evolution of temperature due to heat conduction as well as the convective term, and v_s accounts for the shift in reference frame [42]. The right hand side of this heat equation incorporates the contribution of heat sources and sinks through the volumetric heating rate $Q(x, T)$. The evolution of the temperature inside the material is initially driven by the volumetric heating term as well as the boundary conditions of the particular problem. Heat exchanges due to convection and radiation at the surface can be accounted for in the boundary conditions of the particular problem [42].

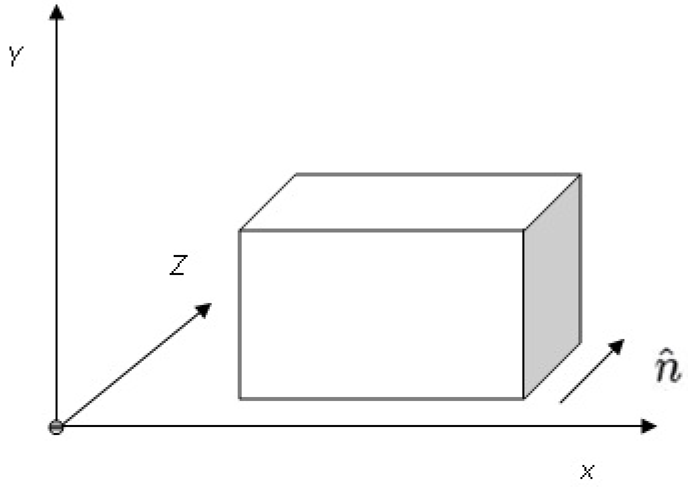

Figure 3.4: Solid in a Three dimensional Space

Considering a solid in a three-dimensional space with a volume (V) and surface area (S) as shown in Fig. 3.4, the Fourier's law of heat conduction is given by;

$$\mu_f = -k \nabla T . \hat{n} \tag{3.2}$$

where ∇ is a function of $(\frac{\partial}{\partial x}, \frac{\partial}{\partial y}, \frac{\partial}{\partial Z})$, T is the temperature, k is thermal conductivity, and μ_f is the heat flux [42].

From law of conservation of energy;

$$\frac{d}{dt}\int_V \rho_{th} dV = -\int_S \mu_f dS + \int_V Q_s dV \tag{3.3}$$

where ρ_{th} is the thermal energy density, and Q_s is the heat source [42]. Thermal energy density is given by;

$$\rho_{th} = C_p \rho T \tag{3.4}$$

where C_p is the specific heat capacity of the material and $C_p\rho$ is a measure of volumetric heat capacity [42]. Equation 3.3 can be simplified further as;

$$\int_V C_p \rho \frac{\partial T}{\partial t} = \int_S k \nabla T . \hat{n} dS + \int_V Q_s dV \tag{3.5}$$

Thus;

$$C_p \rho \frac{\partial T}{\partial t} = k \nabla^2 T + Q_s \tag{3.6}$$

The measure of thermal diffusivity, α, is given by [42];

$$\alpha = \frac{k}{C_p \rho} \tag{3.7}$$

Equation 3.6 can be simplified as;

$$\nabla^2 T + Q = \frac{1}{\alpha}\frac{\partial T}{\partial t} \tag{3.8}$$

where Q and α are constants [42]. For the Solid heating phase, the three-dimensional transient heat conduction equation is given by;

$$\frac{\partial^2 T_{wp}}{\partial x^2} + \frac{\partial^2 T_{wp}}{\partial y^2} + \frac{\partial^2 T_{wp}}{\partial Z^2} + Q = \frac{1}{\alpha_{wp}}\frac{\partial T_{wp}}{\partial t} \tag{3.9}$$

where x, y, and z are spatial variables. $T(x, y, z, t)$ is a function of the spatial variables and time. The heat conduction equation can be re-written as [42]:

$$\nabla^2 T_{wp} + Q = \frac{1}{\alpha_{wp}}\frac{\partial T_{wp}}{\partial t} \tag{3.10}$$

The boundary and initial conditions are;

$$T_{wp}(x, y, z, 0) = T_o \tag{3.11}$$

$$I_{abs} = -k_{wp}\nabla^2 T_{wp} \tag{3.12}$$

3.4 Laser-material interaction process modeling

Ultrashort-pulsed lasers first excite the charge carriers (electron-hole pairs) in semiconductors while their energy is subsequently transferred to the lattice. The model assumes an equal number of electron and holes in the solid and no electron photoemission is considered after the laser irradiation [43, 44].

The evolution of the density of state N, carrier temperature T_c and lattice temperature T_l are derived using the carrier, carrier energy and lattice heat balance equations. Based on this, the temperature and particle dynamics can be derived as [43, 44]:

$$\left.\begin{aligned} C_c\frac{\partial T_c}{\partial t} &= \vec{\nabla}\cdot((k_e+k_h)\vec{\nabla}T_c)-\frac{C_c}{\tau_e}(T_c-T_l)+S(\vec{r},t)\\ C_l\frac{\partial T_l}{\partial t} &= \vec{\nabla}\cdot(k_l\vec{\nabla}T_l)+\frac{C_c}{\tau_e}(T_c-T_l)\\ \frac{\partial N}{\partial t} = \frac{\alpha}{hv}\Omega I(\vec{r},t)+\frac{\beta}{2hv}\Omega^2 I^2(\vec{r},t) &-\gamma N^3+\theta N-\vec{\nabla}\cdot\vec{J}\\ \Omega &= \frac{1-R(T_l)}{\cos\varphi} \end{aligned}\right\} \tag{3.13}$$

where C_c and C_l are the heat capacity of electron-hole pairs and lattice, respectively, v is the frequency of the laser beam, k_e and k_h are the thermal conductivity of the electrons and holes, respectively, k_l is the thermal conductivity of the lattice, h is the Planks constant,Ω is the collision frequency of particles γ is the Auger recombination coefficient, θ is the impact ionization coefficient, α and β are the one-photon and two-photon absorption coefficients, φ is the angle of the incident beam with respect to the normal axis on the irradiated surface, $R(T_l)$ is the reflectance of silicon, t_e is the energy relaxation time, $\vec{J}$ is the carrier current vector and scattering potential $S(\vec{r},t)$ is expressed as [43, 44]:

$$\begin{aligned} S(\vec{r},t) = (\alpha+\Theta N)\Omega I(\vec{r},t)+\beta\Omega^2 I^2(\vec{r},t) &- \frac{\partial N}{\partial t}(E_g+K_bT_c)\\ -N\frac{\partial E_g}{\partial T_1}\frac{\partial T_1}{\partial t} &- \vec{\nabla}\cdot((E_g+4K_BT_c)\vec{J}) \end{aligned} \tag{3.14}$$

where Θ is the free-carrier absorption cross section, K_b is the Boltzmann's constant and E_g the band-gap energy.

The contribution of the current vector in the balance equation for the electron-hole carriers depends largely on the pulse duration. The laser intensity I, in Equations 3.13

and 3.14, is obtained by considering the propagation loss due to one-, two- photon and free carrier absorption [43, 44].

3.5 Interaction of laser with a crystalline solid

The semi-classical heat equation for the laser-solid interaction will be applied in solving the model. The term semiclassical heat equation is due to the introduction in the source term of quantum phenomena such as absorption of n_{ph} photon [20, 45, 46]. Assume the solid has a layered structure, each layer having a linear form for the thermal conductivity. The mathematical statement of the problem can be written as follows [47]:

$$\frac{1}{k(x)}\frac{\partial}{\partial X}(k(x)\frac{\partial T}{\partial X}) + \frac{\partial^2 T}{\partial Y^2} + \frac{\partial^2 T}{\partial Z^2} = -\frac{f(x,y,z,t)}{k(x)} \tag{3.15}$$

where k is the thermal conductivity of the sample and γ is the thermal diffusivity of the sample. $k_i(x) = k(x_1)+m_i(x-x_i)$, $x \in [x_1, x_1+1]$ with , i = 0,1,2,..., n-1. Suppose that the source term: $f(x,y,z,t) = f(x,y,z).[h(t) - h(t-t_0)]$ and the boundary conditions at the interfaces are [48]:

$$\left.\begin{aligned}
T_{i-1,j,k,l}(x,y,z,t)|_{x=x_i} &= T_{i,j,k,l}(x,y,z,t)|_{x=x_i} \\
T_{i+1,j,k,l}(x,y,z,t)|_{x=x_{i+1}} &= T_{i,j,k,l}(x,y,z,t)|_{x=x_{i+1}} \\
k_{i-1}.T_{i-1,j,k,l'}(x,y,z,t)|_{x=x_i} &= k_i.T_{i,j,k,l'}(x,y,z,t)|_{x=x_i} \\
k_{i+1}.T_{i+1,j,k,l'}(x,y,z,t)|_{x=x_{i+1}} &= k_i.T_{i,j,k,l'}(x,y,z,t)|_{x=x_{i+1}}
\end{aligned}\right\} \tag{3.16}$$

where h is the step function and t_0 is the initial time. For describing the interaction between laser beam and crystalline solid, the most general form of interaction is considered [49].

Consider the n-photon absorption phenomena, where n_{ph} can vary from 1 to n_{max}. The multi-photon absorption can be described by the Beer-Lambert law [50]:

$$\frac{dI}{dx} = -\sum_{n_{ph}} \alpha_{n_{ph}} I^{n_{ph}} \tag{3.17}$$

where $\alpha_{n_{ph}}$ is the n-photon absorption coefficient, I is the light flux and x is the propagation direction. We have:

$$\alpha_{n_{ph}} = \frac{2W_{n_{ph}} n\hbar w}{I^{n_{ph}}} \tag{3.18}$$

where $I^{n_{ph}}$ is the incident radiation intensity and the factor 2 accounts for electron-spin degeneracy. The $\hbar$ is the reduced Planck's constant and w is the frequency. The n-photon transition probability $W_{n_{ph}}$ is given by the Goppert-Mayer n^{th} order time-dependent perturbation theory [51]. The probability $W_{n_{ph}}$ of a direct electronic transition from an initial valence band to a final conduction band, accompanied by the simultaneous absorption of n photons, is expressed by [52]:

$$W_{n_{ph}} = \frac{2\Pi}{\hbar} \int | \sum_{m} \sum_{l} \cdots \sum_{j} \sum_{i} \frac{\langle\psi_c|H|\psi_m\rangle\langle\psi_m|H|\psi_i\rangle}{[E_m - E_l - (n-1)\hbar w]} ..$$

$$.. \frac{\langle\psi_m|H|\psi_i\rangle}{E_j - E_i - 2\hbar w} . \frac{\langle\psi_m|H|\psi_i\rangle}{E_i - E_v - 2\hbar w} |^2 \tag{3.19}$$

$$\times \delta[E_c(\overrightarrow{k}) - E_v(\overrightarrow{k}) - n\hbar w] \frac{d^3\overrightarrow{k}}{(2\Pi)^3}$$

where: ψ_i, ψ_j... are the Bloch functions of the crystalline electrons in bands i, j,...,with energies E_i, E_j,...,etc. The $\overrightarrow{k}$ integration is over the entire first Brillouin zone and H is the Hamiltonian interaction.

3.6 Crack propagation

The theoretical strength of material, in terms of stress, can be estimated from the work necessary to increase the atomic intraplane distance by 25 percent at which cleaving of a crystal occurs [53]:

$$\sigma_{th} = \sqrt{\frac{\gamma E}{a_o}} \simeq \frac{E}{2\pi} \tag{3.20}$$

where E is the Young modulus, γ is the surface energy per unit area and a_o is the atomic intraplane distance. When crack is present inside material, the stress at the crack tip depends on the crack shape and size [53]:

$$\sigma_{max} = 2\sigma\sqrt{\frac{l_c}{l_p}} \tag{3.21}$$

where l_c is half the length of the crack (assumed to be elliptical), σ is the applied stress and l_p is the radius at the crack tip. Crack propagation ensues at the fracture stress when σ_{th} =σ_{max} [54].

3.7 Summary

In this chapter, the major assumptions on which the numerical model was based were discussed. The heat equation was discussed. A mathematical model for predicting the pulsed laser matter interaction process was presented. It is difficult to experimentally predict laser machining attributes such as heat extent, thermal stresses and kerf depths.

In the laser micromachining system, the material is broken down into a mesh and the PDE is investigated at nodes in the mesh . The size of the meshing determines how many nodes will lie within the geometry. This solution can be done analytically, which will give more precise answers and will involve using the solution of the PDE at one node to determine the solution for the PDE at the following node. However, this is time consuming and tedious.

Mathematical simulation methods based on suitable physical computational models are a good approach in analyzing laser micromachining. Mathematical models give the advantage of checking the physical model, estimating important parameters and calculating the effect of varying any parameter. Current numerical models are obtained under simplified conditions and can be used to qualitatively conceptualize the main features of the thermal laser to material interaction process. It is, therefore, reasonable to perform the laser micromachining process numerically. By use of computers, computational time is greatly reduced.

CHAPTER FOUR

4.0 NUMERICAL SOLUTION OF LASER MICROMACHINING MODEL

4.1 Introduction

This chapter provides the numerical method solutions to the governing equations of heat transfer in three dimensions. Here, only steady states effects are considered. The finite element method is discussed. The system assembly and boundary conditions are discussed . The unknown dependent variables, temperature, volumetric heating rate and heat flux are determined at selected grid points in the computational domain. Presented also is the method for selecting the optimal laser beam and process parameters. The model solution discussed the simulation steps required to set up the model in the $COMSOL^R$ FEA software. The procedure for validation was also discussed.

4.2 Modeling heat transfer in three dimensions

The governing equation for heat transfer in three dimensions can be written as follows:

$$\frac{\partial}{\partial x}\Big(k_x\frac{\partial T}{\partial x}\Big)+\frac{\partial}{\partial y}\Big(k_y\frac{\partial T}{\partial y}\Big)+\frac{\partial}{\partial z}\Big(k_z\frac{\partial T}{\partial z}\Big)+Q=0 \tag{4.1}$$

where only conduction effects are included and steady-state conditions are assumed [55]. Figure 4.1 shows a representation of the work piece orientation. In this three-dimensional case, convection effects are treated as boundary conditions [56]. The following boundary conditions are be taken into account:

1. Convective boundary conditions will be used at the top of the surface where both laser heating and ambient air cooling take place.
2. The remaining boundaries are thermally insulated.

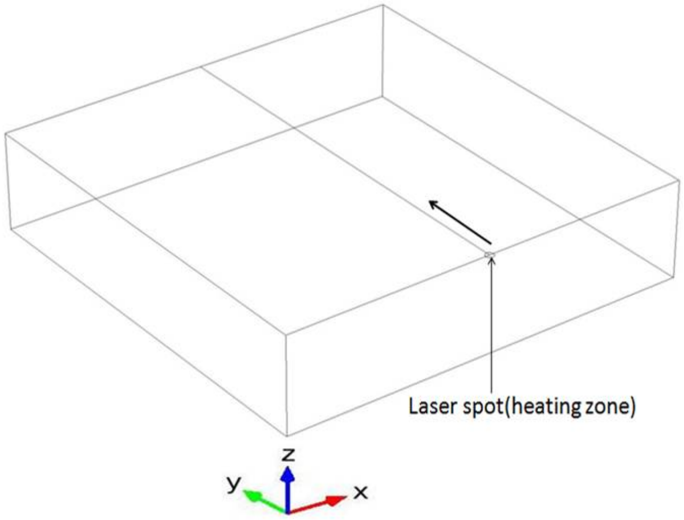

Figure 4.1: Orientation of the axes with respect to the work piece.

The domain to which Equation 4.1 applies is represented by a mesh of finite elements as shown in Figure 4.2, in which the temperature distribution is discretized as:

$$T(x,y,z) = \sum_{i=1}^{M} N_i(x,y,z)T_i = [N]\{T\} \tag{4.2}$$

where M is the number of nodes per element. $N_i(x,y,z)$ is the interpolation function associated with nodal temperature T_i, [N] is the row matrix of interpolation functions and $\{T\}$ is the column matrix (vector) of nodal temperature for the nodes [55].

The standard Galerkin approach states that the variational temperature, ∂T is interpolated with the same functions as temperature [55]. Application of the Galerkin method

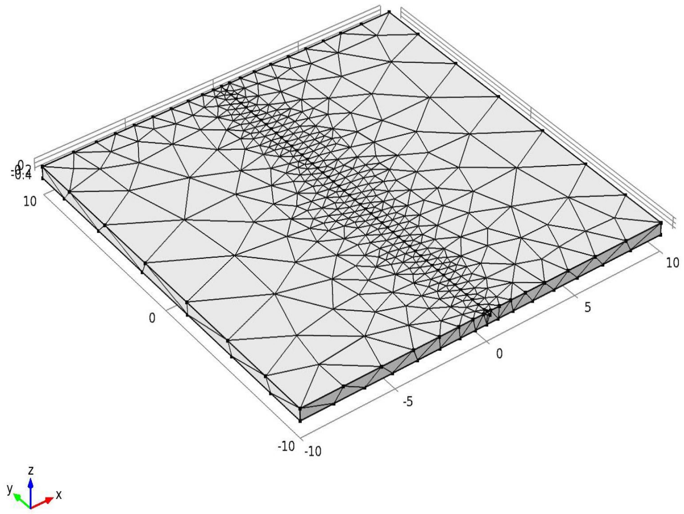

Figure 4.2: A mesh of finite elements.

to Equation 4.1 results in M residual equations:

$$\left.\begin{aligned} \int\int\int_V \left[\frac{\partial}{\partial x}\left(k_x\frac{\partial T}{\partial x}\right)+\frac{\partial}{\partial y}\left(k_y\frac{\partial T}{\partial y}\right)+\frac{\partial}{\partial z}\left(k_z\frac{\partial T}{\partial z}\right)+Q\right]N_i dV = 0 \\ \\ i = 1, ..., M \end{aligned}\right\} \tag{4.3}$$

where V is element volume [55].

The derivative terms for Equation 4.3 are expressed as [55]:

$$\left.\begin{aligned} \frac{\partial}{\partial x}\left(k_x\frac{\partial T}{\partial x}\right)N_i &= \frac{\partial}{\partial x}\left(k_x\frac{\partial T}{\partial x}N_i\right) - k_x\frac{\partial T}{\partial x}\frac{\partial N_i}{\partial x} \\ \\ \frac{\partial}{\partial y}\left(k_y\frac{\partial T}{\partial y}\right)N_i &= \frac{\partial}{\partial y}\left(k_y\frac{\partial T}{\partial y}N_i\right) - k_y\frac{\partial T}{\partial y}\frac{\partial N_i}{\partial y} \\ \\ \frac{\partial}{\partial z}\left(k_z\frac{\partial T}{\partial z}\right)N_i &= \frac{\partial}{\partial z}\left(k_z\frac{\partial T}{\partial z}N_i\right) - k_z\frac{\partial T}{\partial z}\frac{\partial N_i}{\partial z} \end{aligned}\right\} \tag{4.4}$$

Hence the residual equations become [55]:

$$\left.\begin{aligned} &\int\int\int_V \Big[\frac{\partial}{\partial x}\Big(k_x\frac{\partial T}{\partial x}N_i\Big)+\frac{\partial}{\partial y}\Big(k_y\frac{\partial T}{\partial y}N_i\Big)+\frac{\partial}{\partial z}\Big(k_z\frac{\partial T}{\partial z}N_i\Big)\Big]dV \\ &+\int\int\int_V QN_i dV=\int\int\int_V\Big(k_x\frac{\partial T}{\partial x}\frac{\partial N_i}{\partial x}+k_y\frac{\partial T}{\partial y}\frac{\partial N_i}{\partial y}+k_z\frac{\partial T}{\partial z}\frac{\partial N_i}{\partial z}\Big)dV \\ &i=1,...,M \end{aligned}\right\} \tag{4.5}$$

The integral on the left side of Equation 4.5 contains a perfect differential in three dimensions and can be replaced by an integral over the surface of the volume using Greens theorem in three dimensions: If F(*x*,*y*,*z*), G(*x*,*y*,*z*)and H(*x*,*y*,*z*)are functions defined in a region of *xyz* space (the element volume in our context), then

$$\int\int\int_V\Big(\frac{\partial F}{\partial x}+\frac{\partial G}{\partial y}+\frac{\partial H}{\partial z}\Big)dV=\oint\oint_A(Fn_x+Gn_y+Hn_z)dA \tag{4.6}$$

where A is the surface area of the volume and n_x, n_y, n_z are the Cartesian components of the outward unit normal vector of the surface area [55]. This theorem is the three dimensional counterpart of integration by parts [55].

Fourier? law of heat conduction in x, y and z plane is expressed as:

$$\left.\begin{aligned} q_x&=-k_x\frac{\partial T}{\partial x}\\ q_y&=-k_x\frac{\partial T}{\partial y}\\ q_z&=-k_x\frac{\partial T}{\partial z}\end{aligned}\right\} \tag{4.7}$$

Using Fourier's law and comparing Equation 4.6 to the first term of Equation 4.5, we obtain Equation 4.8 [55].

$$\left.\begin{aligned} &-\oint\oint(q_x n_x + q_y n_y + q_z n_z)N_i dA + \int\int\int_V Q N_i dV \\ &= \int\int\int_V \Big(k_x \frac{\partial T}{\partial x}\frac{\partial N_i}{\partial x} + k_y \frac{\partial T}{\partial y}\frac{\partial N_i}{\partial y} + k_z \frac{\partial T}{\partial z}\frac{\partial N_i}{\partial z}\Big) dV \\ &\qquad\qquad\qquad\qquad\qquad\qquad\qquad\qquad i = 1, ..., M \end{aligned}\right\} \tag{4.8}$$

Rearranging the the nodal temperatures [T] and the interpolation functions [N] in Equation 4.8 results to Equation 4.9 which represents a system of M algebraic equations in the M unknown nodal temperatures T [55]:

$$\left.\begin{aligned} &\int\int\int_V \Big(k_x \frac{\partial [N]}{\partial x}\frac{\partial N_i}{\partial x} + k_y \frac{\partial [N]}{\partial y}\frac{\partial N_i}{\partial y} + k_z \frac{\partial [N]}{\partial z}\frac{\partial N_i}{\partial z}\Big) \{T\} dV \\ &= -\oint\oint_A (q_x n_x + q_y n_y + q_z n_z)N_i dA + \int\int\int_V Q N_i dV \\ &\qquad\qquad\qquad\qquad\qquad\qquad\qquad\qquad i = 1, ..., M \end{aligned}\right\} \tag{4.9}$$

The system of equations for the three dimensional element formulation is expressed by Hutton [55]:

$$\left.\begin{aligned} &\int\int\int_V \Big(k_x \frac{\partial [N]^T}{\partial x}\frac{\partial [N]}{\partial x} + k_y \frac{\partial [N]^T}{\partial y}\frac{\partial [N]}{\partial y} + k_z \frac{\partial [N]^T}{\partial z}\frac{\partial [N]}{\partial z}\Big) dV \{T\} \\ &= \int\int\int_V Q[N]^T dV - \oint\oint_A (q_x n_x + q_y n_y + q_z n_z)[N]^T dA \end{aligned}\right\} \tag{4.10}$$

and Equation 4.8 can be represented in the desired matrix form as [55]:

$$[k^{(e)}]\{T^{(e)}\} = \{f_Q^{(e)}\} + \{f_q^{(e)}\} \tag{4.11}$$

Comparing the last two equations, that is, Equation 4.10 and Equation 4.11, the element conductance (stiffness) matrix is:

$$[k^{(e)}] = \int\int\int_V \Big(k_x \frac{\partial[N]^T}{\partial x}\frac{\partial[N]}{\partial x} + k_y \frac{\partial[N]^T}{\partial y}\frac{\partial[N]}{\partial y} + k_z \frac{\partial[N]^T}{\partial z}\frac{\partial[N]}{\partial z}\Big) dV \tag{4.12}$$

The element force vector representing internal heat generation is:

$$\{f_Q^{(e)}\} = \int\int\int_V Q[N]^T dV \tag{4.13}$$

and the element nodal force vector associated with heat flux across the element surface area is [55]:

$$\{f_q^{(e)}\} = -\oint\oint_A (q_x n_x + q_y n_y + q_z n_z)[N]^T dA \tag{4.14}$$

4.3 System assembly and boundary conditions

The procedure for assembling the global equations for a three-dimensional model for heat transfer analysis is identical to that of a one or two dimensional problems. The element type is selected based primarily on geometric considerations. The volume is then divided into a mesh of elements by first defining nodes in the global coordinate system throughout the volume, then each element by the sequence and number of nodes required for the element type. Element-to-global nodal correspondence relations are then determined for each element and the global stiffness matrix is assembled.

Similarly, the global force vector is assembled by adding element contributions at nodes common to two or more elements. The global force vector procedure is straightforward in the case of internal generation, as given by Equation 4.13. However, in the case of the element gradient terms, that is, Equation 4.14, the procedure is best described in terms of the global boundary conditions.

Three types of boundary conditions exist: the specified temperatures, the specified heat flux and the convection conditions. In the first case, specified temperatures are taken into account by reducing the system equations. This is achieved through inserting the known nodal temperatures into the system equations. The latter two cases involve only elements that have surfaces (element faces) on the outside surface of the global volume. As an illustration, Figure 4.3a shows two brick elements that share a common face in an assembled finite element model. For convenience, the common face perpendicular to the x axis is taken. In Figure 4.3b, the two elements are shown separately with the associated normal vector components identified for the shared faces.

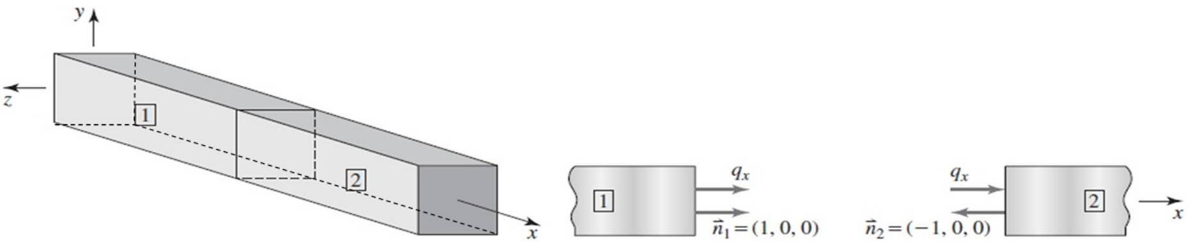

(a) Common face in two 3-D elements.

(b) Edge view of common face.

Figure 4.3: Cancelation of conduction gradient terms.

For steady-state heat transfer, the heat flux across the face is the same for each element and since the unit normal vectors are opposite, the gradient force terms cancel out. The result is analogous to internal forces in a structural problem via Newton's third law of action and reaction. Therefore, on inter-element boundaries, which are areas for three-dimensional elements, the resultant of the element force terms defined by Equation 4.14

is zero in the global assembly process. The element surface areas that are part of the surface area of the volume being modeled have different considerations. Generally, these outside areas are subjected to convection conditions. For such convection boundary conditions, the flux conditions of Equation 4.14 must be in balance with the convection from the area of concern. Mathematically, the condition is expressed as:

$$\begin{aligned}\{f_q^{(e)}\} = -\oint\oint_A (q_x n_x + q_y n_y + q_z n_z)[N]^T dA = -\oint\oint_A (q_n n)[N]^T dA \\ = -\oint\oint_A h(T^{(e)} - T_a)[N]^T dA\end{aligned} \tag{4.15}$$

4.4 Optimization

In this research, optimal laser machining parameters are considered to be those parameters that result in the least heat affected zone and the least induced thermal stress. The material studied is monocrystalline silicon. The desired machining attribute studied in this research is the resulting material kerf depth and microcrack formation. Optimal parameters are determined by means of observation and analysis of results. For example, if it is desired to produce a through hole in monocrystalline silicon by means of laser drilling, then, it would be prudent to select the right power, or scan speed or spot size that result in the least extent of melt affected area and the least microcrack formation.

4.5 Model solution

The solution of the model of the characteristic of the material due to the laser cutting action was accomplished using $COMSOL^R$, which is a Finite Element Analysis software package that allows the user to develop 3D models with associated boundary conditions. In this research, $COMSOL^R$ was used for simulation purposes to mathematically model appropriate heat transfer physics and thermal stress analysis. $IMAGE^R$, an image analyzer, was used to analyze the images generated from $COMSOL^R$. The data from the images was used to construct graphs for illustration of resulting kerf depth and microcrack formation.

Finite element analysis uses computer codes. These codes are utilized by designers to investigate the effect of various parameters which would either be difficult to analyze experimentally, or would require very costly tests. Though the computer codes provide a cheap alternative to analyze effects of laser micromachining on materials, their validity must be tested to be sure that the results obtained are within acceptable limits. The code is usually validated by comparing the results obtained from it to existing experimental ones. Setting up simulation involves a series of steps as shown in Figure 4.4

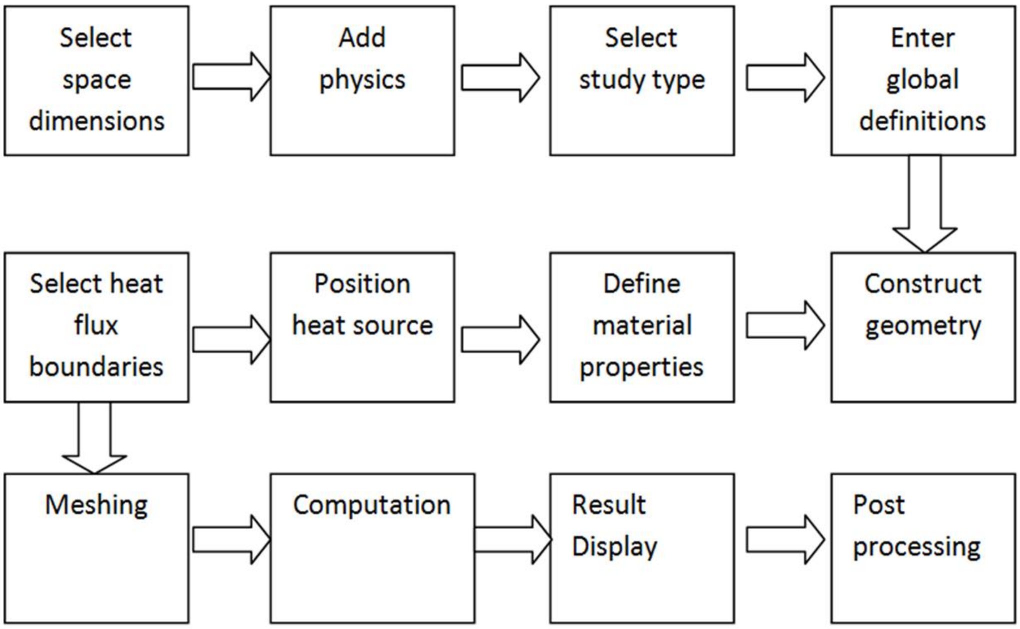

Figure 4.4: Simulation steps for accomplishing the model.

The simulation steps for accomplishing the model in $COMSOL^R$ are shown in Figure 4.4 and are outlined as follows:

1. Select space dimensions: Here, a three dimensional space is selected since the study is in three dimension.
2. Add physics: This gives the option of performing a steady state or time dependent study.
3. Select study type. For this model, heat transfer and thermal stress models study type are selected.
4. Enter global definitions: Here, parameters of the laser machining system are defined, parameters for the geometry and analytic functions for the laser are also defined.
5. Construct geometry: The workpiece dimensions and laser path are designed in three dimension space, laser heat source geometry is modeled.
6. Define material properties: The physical parameters for monocrystalline silicon are defined here.
7. Position heat source: The selection for the boundary where the volumetric laser heat source will act is done here
8. Define heat boundaries: The boundary conditions such as convection boundaries are selected at this stage.
9. Meshing: A tetrahedral fine mesh is constructed and implemented into the model.
10. Computation: The iteration steps for solving the model are selected and model is computed.

11. Result display: Simulation results are displayed in several formats, e.g, graphs, tables and thermal and thermal stress images.
12. Post processing: The analysis of image results is performed at this stage.

4.6 Model Validation

In this study, the results obtained from $COMSOL^R$ were compared with results obtained from experiments. Figure 4.5 shows the machine used for experiments. The experimental setup used an Nd:YAG laser machining system. The laser power of the machine can be changed from 0 to 200 W. A pulsed Nd:YAG laser with the wavelength of $1.06\mu m$ was used for cutting simulation. The numerical results are compared to experimental data for validity. The physical parameters for monocrystalline silicon

Figure 4.5: Nd:YAG laser machine.

investigated are listed in the Table 4.1.

Table 4.1: Physical Properties of Monocrystalline Silicon

Property, **symbol(unit)**	**Value**
Melting temperature, T_m(K)	1683
Normal boiling temperature, T_b(K)	3514
Critical point temperature, T_{cr}(K)	5159
Liquid density, $\rho_l(kgm^{-3})$	2520
Solid density, $\rho_s(kgm^{-3})$	2320
Latent heat of vaporization,$L_v(Jkg^{-1})$	1.3722×10^7
Latent heat of fusion,$L_m(Jkg^{-1})$	1.797×10^6
Solid constant-pressure specific heat, $c_{ps}(Jg^{-1}K)$	$0.694 \exp(2.375 \times 10^{-4}T)$
Liquid constant-pressure specific heat, $c_{pl}(Jg^{-1}K)$	1050
Laser beam absorptivity for flat surface	0.66 for solid, 0.27 for liquid

4.7 Summary

This chapter discussed the numerical solutions to the governing equations and the related boundary conditions. The modeling of heat transfer in three dimension was derived. The model implementation by use of Finite Element Analysis software $COMSOL^R$ was also presented. The procedure for parameter optimization was discussed. The procedure was result validation was also presented.

CHAPTER FIVE

5.0 RESULTS AND DISCUSSION

In this chapter, simulation results are presented and compared to experimental results from previous researchers. The laser machining parameters investigated include: scan speed, laser spot size and power.

5.1 Simulation results

5.1.1 Effect of scan speed

The moving pulsed laser parameters used for the simulation to determine the effect of scan speed on material temperature and thermal stress are listed in Table 5.1.

Table 5.1: Parameters used for the simulation of scan speed.

Parameter	**Value**
Laser power	100 W
Pulse width	10 ns
Spot diameter	0.4 mm
Wafer thickness	0.5 mm

5.1.1.1 Temperature field analysis

Figure 5.1 shows the surface temperatures of the material at the laser spot for the various scan speeds. The temperature rapidly increases during laser irradiation.

For a scan speed of 100 mm/s (Figure 5.1a), the maximum temperature of the center of the laser spot reaches 5300 K which is beyond silicon critical temperature of 5159 K. For a scan speed of 200 mm/s (Figure 5.1b), the maximum temperature of the

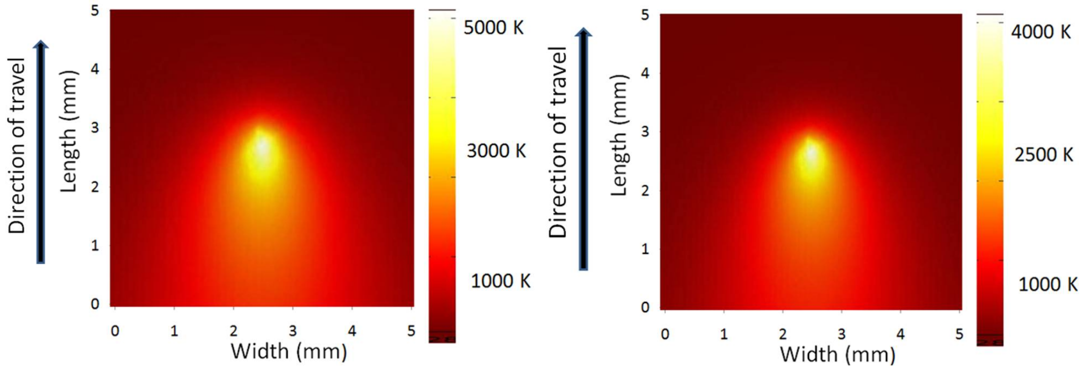

(a) v=100 mm/s

(b) v=200 mm/s

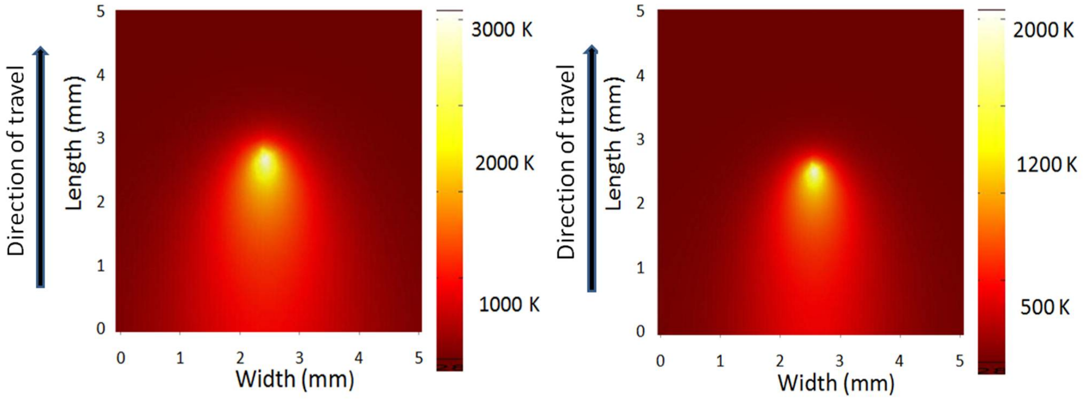

(c) v=300 mm/s

(d) v=400 mm/s

Figure 5.1: Surface temperatures of the material for different scan speeds.

material at the center of the laser spot reaches 4000 K which is beyond silicon boiling temperature of 3514 K.

For a scan speed of 300 mm/s (Figure 5.3c), the maximum temperature of the center of the laser spot reaches 3200 K, which is below silicon boiling temperature of 3514 K, but way above melting point of 1683 K. For a scan speed of 400 mm/s (Figure 5.1d), the maximum temperature of the center of the laser spot reaches 2500 K, which is below silicon boiling temperature of 3514 K, but above melting point of 1683 K.

Figure 5.2 shows how the material surface temperature at the laser spot compares for various scan speeds. The material temperature at the heating zone is seen to reduce

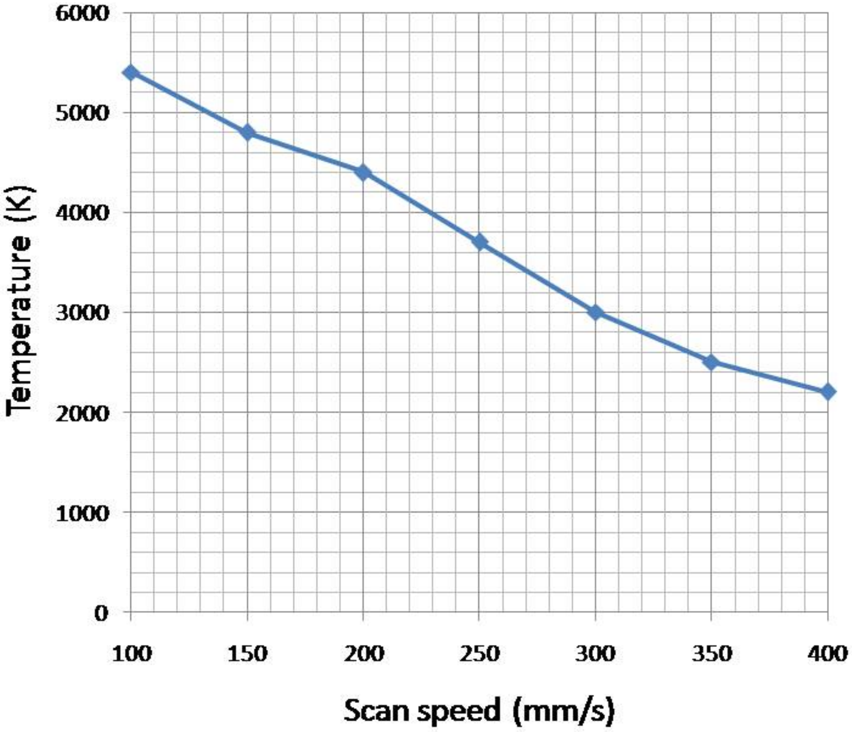

Figure 5.2: Influence of laser scan speed on the material surface temperature at the beam spot.

(5300 k to 2500k) as the scan speed increases from 100 mm/s to 400 mm/s respectively. This reduction is attributed to the decreasing laser beam resident time at a spot as the scan speed increases. Fast scan speeds will result in slow build up of temperature, provided the heat input is fixed. As the laser moves forward, the temperature on the surface left behind drops. This happened due to the convection of heat to the surface ambient. The convection occurs due to the temperature gradient that exist between the heated material and the ambient at 273 k. Also, heat transfer from the heating zone towards the bulk material by conduction occurs radially into the material and this contributes to the temperature drop.

Figure 5.3 shows the temperature distribution along the material thickness for the various laser scan speeds. Figure 5.4 shows the kerf profile along material thickness for

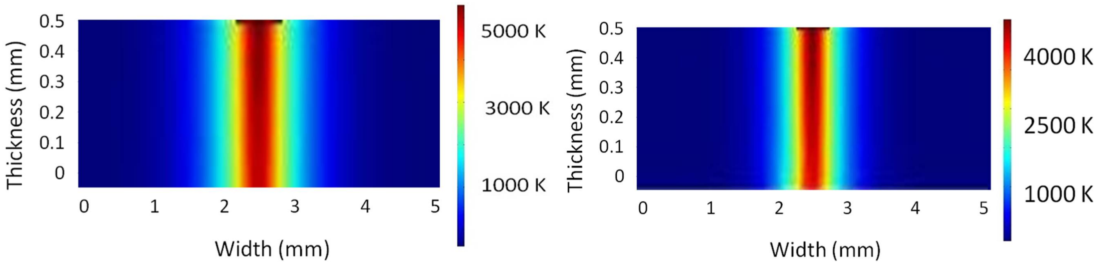

(a) v=100 mm/s

(b) v=200 mm/s

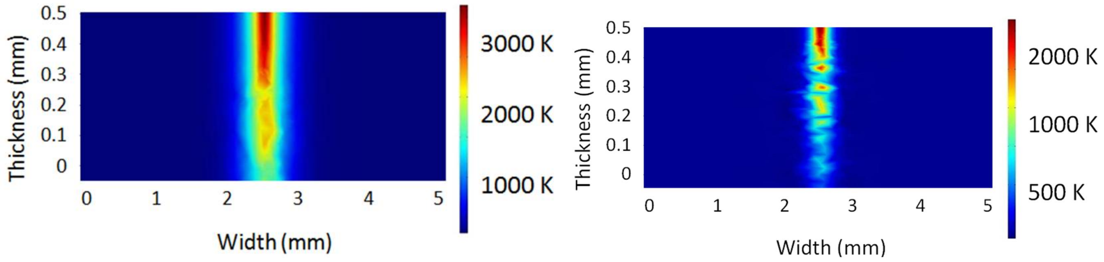

(c) v=300 mm/s

(d) v=400 mm/s

Figure 5.3: Temperature distribution along the material thickness for different scan speeds.

different laser scan speeds.

For the scan speed of 100 mm/s (Figure 5.3a), the temperature of the material below the beam spot (heating zone) reaches over 5200 K. The whole thickness of the material below the heating zone is totally ablated. The zone closest to the heating zone reaches temperatures over 3500 K which is past silicon boiling point of 3514 K. This will cause the region close to the heating zone to melt. The laser cuts through the material thickness, as shown in Figure 5.4a. This scan speed can be used for micromachining through silicon. However, this scan speed is not optimal for the micromachining of this workpiece, due to the extensive melting caused.

For the scan speed of 200 mm/s (Figure 5.3b), the temperature of the material below the beam spot reaches 4000 K. The heating zone reaches boiling point and is evaporated. The region close to the heating zone reaches temperatures up to 2000 K. This zone therefore experiences melting since the temperatures reached here surpass the

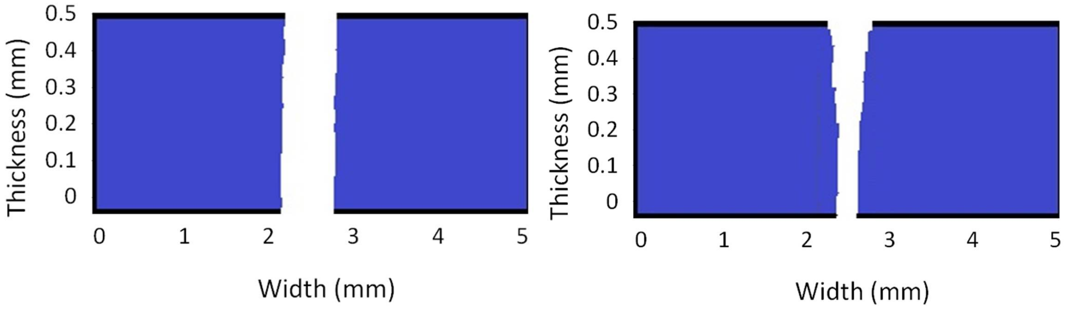

(a) v=100 mm/s (b) v=200 mm/s

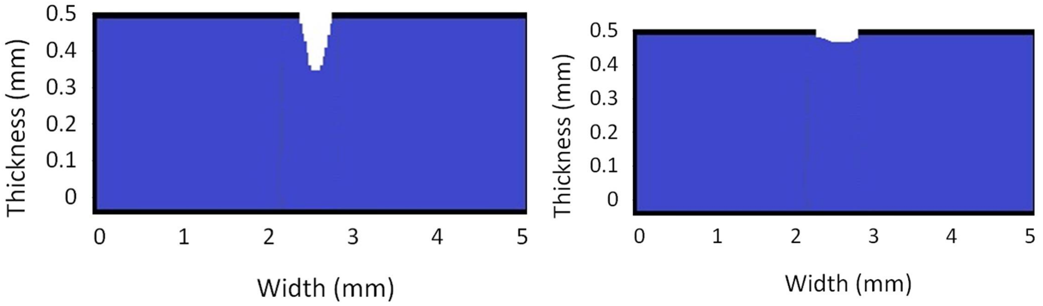

(c) v=300 mm/s (d) v=400 mm/s

Figure 5.4: Kerf profile along material thickness for different laser scan speeds.

silicon melting temperature of 1683 K. The melting of the region close to the heating zone is not as extensive as for the 100 mm/s scan speed. The laser cuts through the material thickness, as shown in Figure 5.4b. This scan speed is the optimal choice for micromachining through silicon.

For the scan speed of 300 mm/s (Figure 5.3c), the temperature of the material below the beam spot reaches 3400 K. For the scan speed of 400 mm/s (Figure 5.3d), the temperature of the material below the beam spot reaches 2800 K. The heating zone reaches melting point but does not reach boiling point. For both scan speeds, the region close to the heating zone reaches temperatures up to 1500 K, which is below the melting point of silicon. For both speeds, the laser does not cut through material thickness. The resulting kerf depths are as shown in Figures 5.4c and 5.4d respectively. Both these speeds result to minimal melting of the regions close to the heating zones.

These scan speeds is optimal for microchannel machining in silicon.

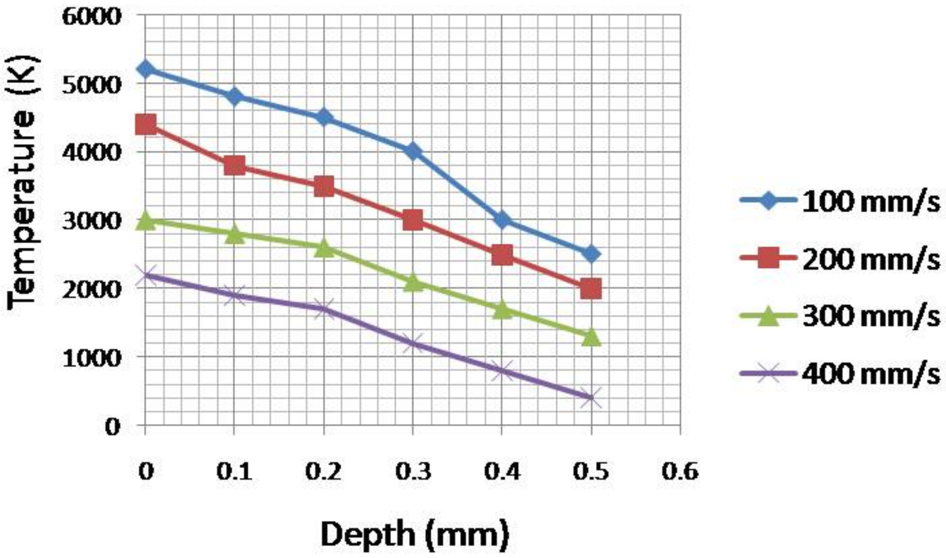

Figure 5.5: Temperature profiles along material depth for different laser scan speeds.

Figure 5.5 shows the temperature profiles along the material depth for different scan speeds. The temperature is seen to generally reduce through the depth of the work piece. The mean temperature drop between between the top surface and the bottom surface of the workpiece is 1500 K for all the four scan speeds. The temperature difference results in heat transfer from the region of high temperature (heating zone) to the regions of low temperature. Three mechanisms of heat transfer take place here. First, the top surface of the workpiece experiences convection heat loss to the ambient at 273 K. Second, heat conduction takes place radially in all directions in the workpiece. Lastly, the region directly below the heating zone is semitransparent and is heated up by the the laser light radiation. As the scan speed increases the energy per unit area decreases. The scan speed also influences the overlapping between subsequent laser pulses, the slower the speed the greater the overlap.

Figure 5.6 shows the influence of laser scan speed on workpiece kerf depth. Slow scan

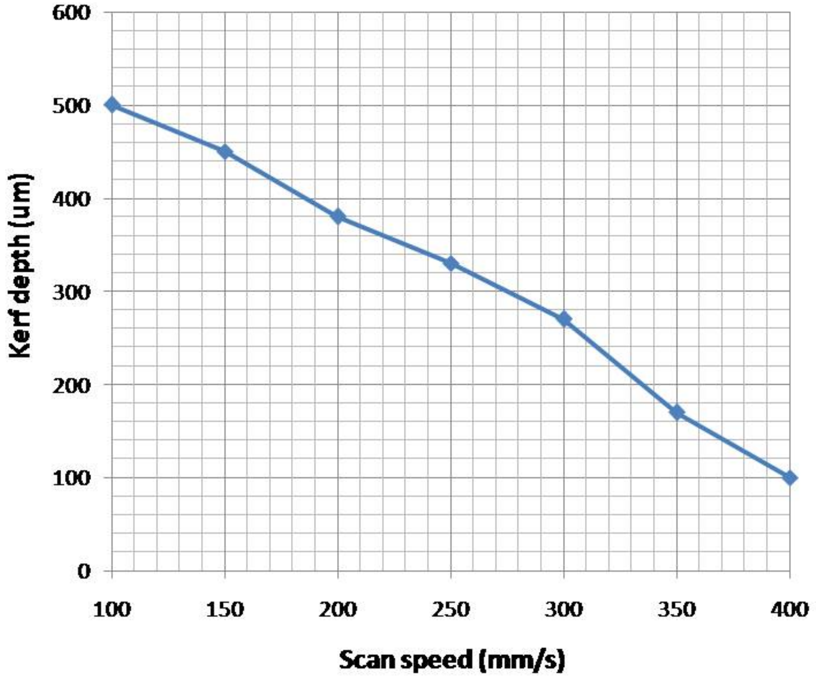

Figure 5.6: Influence of laser scan speed on workpiece kerf depth.

speeds (below 200 mm/s) result in material being cut through the whole thickness. These speeds provided for long beam residence time at a spot. The long residence times allowed for more heat input and absorption into the material. Sufficient heating allowed the material below the heating zone to reach melting point. Scan speed of 300 mm/s results in kerf depth of 0.1 mm. As scan speed increased to 400 mm/s, kerf depth of 0.04 mm resulted. The reduction in kerf depth as scan speeds increase is attributed to the reduction in the beam spot resident time. As the scan speed increases the energy per unit area decreases. The reduced beam spot residence time result in less heat input into the workpiece.The scan speed also influences the overlapping between subsequent laser pulses, the slower the speed the greater the overlap. Insufficient heating result in minimal depths of material below the heating zone reaching melting point.

5.1.1.2 Stress field analysis

Figure 5.7 shows the surface von Mises stress fields for different laser scan speeds. Figure 5.8 shows the von Mises stress distribution field along material thickness for different scan speeds. Figure 5.9 shows the extent of microcracks formation along material thickness for different scan speeds. von Mises stress yield criterion is used for stress analysis. When the maximum von Mises stress exceeds the fracture (yield) stress of silicon, 300 Mpa, microcracks are formed.

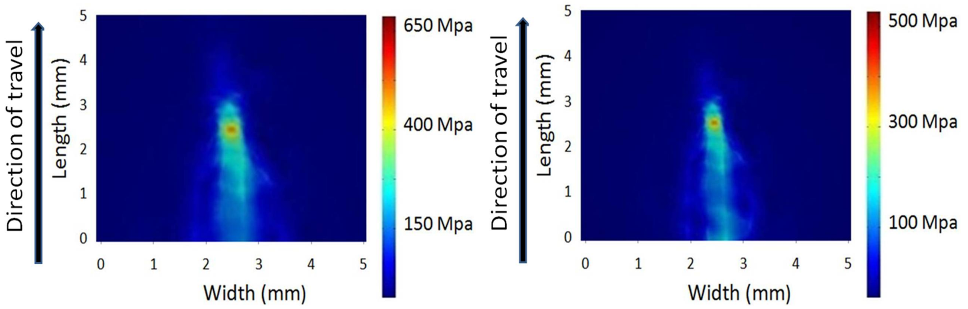

(a) v=100 mm/s (b) v=200 mm/s

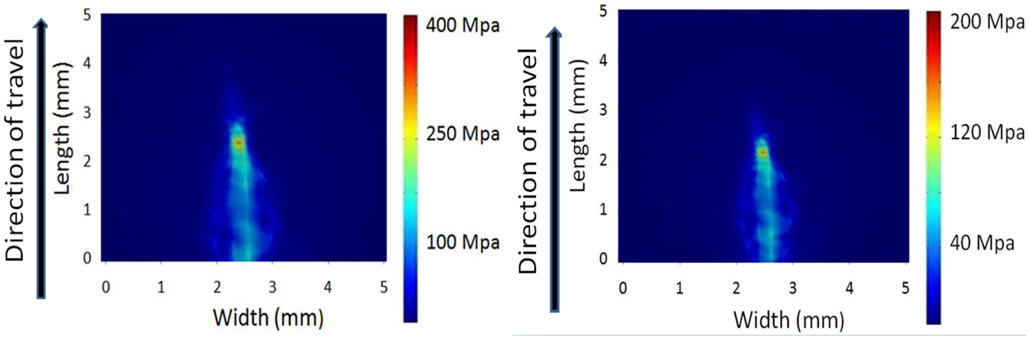

(c) v=300 mm/s (d) v=400 mm/s

Figure 5.7: Surface von Mises stress fields for different laser scan speeds.

At the scan speed of 100 mm/s (Figures 5.7a and 5.8a), stress at the heating zone reaches 650 Mpa. The region closest to the heating zone reaches 400 Mpa. These two zones experience crack formation, since their stresses have exceeded the fracture (yield) stress of silicon (300 Mpa). The stress at the region farthest from the heating

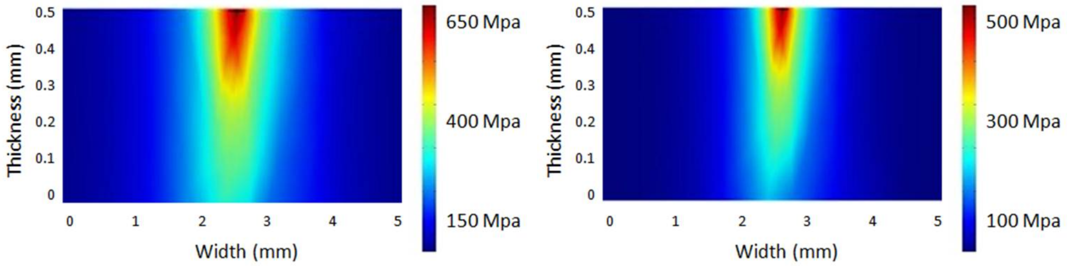

(a) v=100 mm/s (b) v=200 mm/s

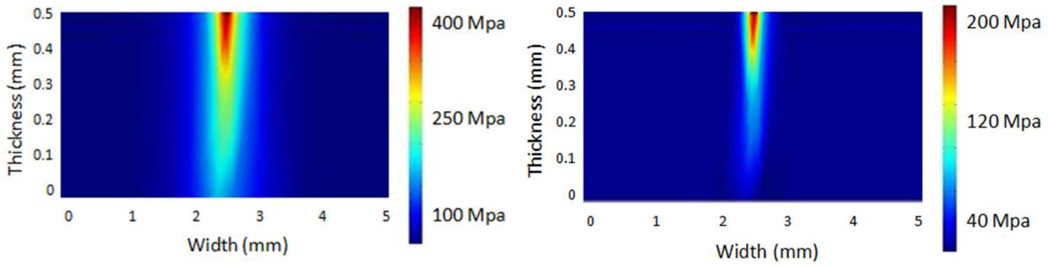

(c) v=300 mm/s (d) v=400 mm/s

Figure 5.8: von Mises stress distribution field along material thickness for different scan speeds.

zone reaches 300 Mpa. Cracks will also form in this zone, as shown in Figure 5.9a. This laser scan speed is not optimal for micromachining monocrystalline silicon since such a speed will result to high thermal stresses within the material and microcrack formation.

At the scan speed of 200 mm/s (Figures 5.7b and 5.8b), stress at the heating zone reaches 500Mpa. The region closest to the heating zone reaches 300 Mpa. These two zones experience crack formation, since their von Mises stresses have exceeded the fracture (yield) stress of silicon (300 Mpa). The stress at the region farthest from the heating zone reaches 100 Mpa. Cracks will not be initiated in this zone, as shown in Figure 5.9b. This laser scan speed is not optimal for micromachining monocrystalline silicon. Such a speed will result in thermal stresses within the material and microcrack formation. Though, 200 mm/s is a better choice than 100 mm/s, since it will result to

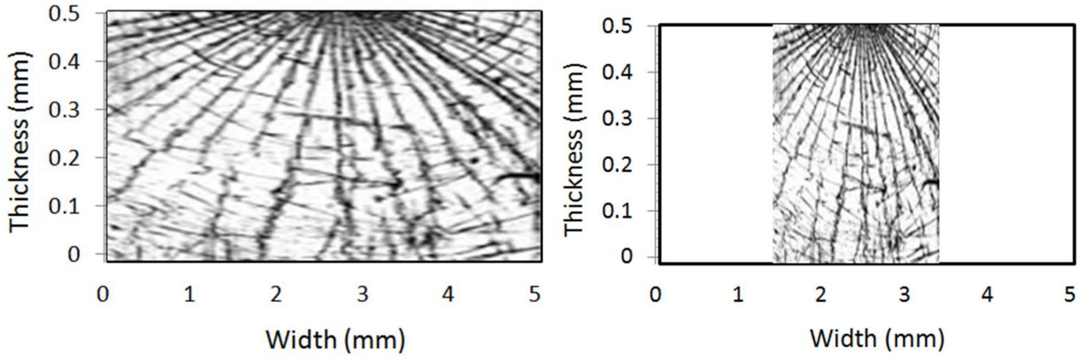

(a) v=100 mm/s (b) v=200 mm/s

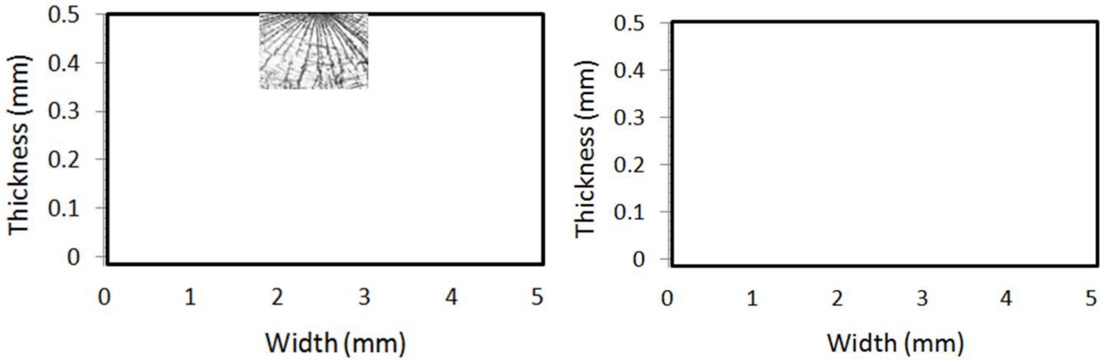

(c) v=300 mm/s (d) v=400 mm/s

Figure 5.9: Extent of microcracks formation along material thickness for different scan speeds.

less microcracking during laser micromachining.

At the scan speed of 300 mm/s (Figures 5.7c and 5.8c), stress at the heating zone reaches 400 Mpa. There is crack formation in this zones since the stress has exceeded 300 Mpa. The stress at the region closest to the heating zone reaches 250 Mpa. The stress at the region farthest from the heating zone reaches 100 Mpa. Cracks is not initiated in these two latter zones, as shown in Figure 5.9c. This laser scan speed is not optimal for micromachining monocrystalline silicon. Such a speed will result in thermal stresses around the heating zone and microcrack formation. The scan speed of 300 mm/s is a better choice than 100 mm/s and 200 mm/s, since it will result to less microcracking during laser micromachining.

At the scan speed of 400 mm/s (Figures 5.7d and 5.8d), stress at the heating zone reaches 200 Mpa. There is no crack formation in this zones since the stress has not exceeded 300 Mpa. The stress at the zone closest to the heating zone reaches 120 Mpa. The stress at the zone farthest from the heating zone reaches 40 Mpa. Cracks is not initiated in these two latter zones, as shown in Figure 5.9d. This laser scan speed is optimal for micromachining monocrystalline silicon. Such a speed will not result in thermal stresses around the heating zone and hence no microcrack formation. The scan speed of 400 mm/s is the optimal choice since it will result to zero microcracking during laser micromachining.

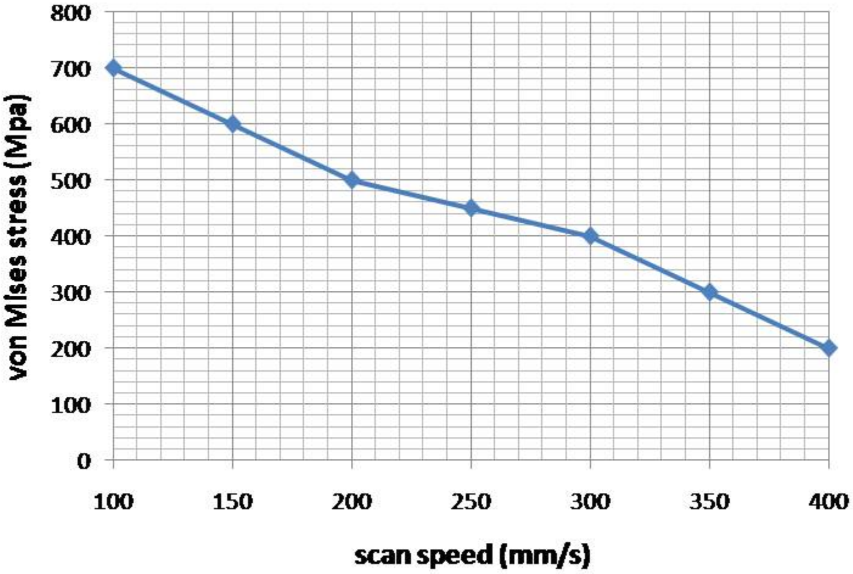

Figure 5.10: Influence of laser scan speed on von Mises stress at the material surface.

Figure 5.10 shows how the maximum von Mises stress at the laser spot on the material surface varies with scan speeds. The stress is seen to generally reduce as the scan speed increases. Scan speed of 100 m/s causes von Mises stress of 700 Mpa. Scan speed of 400 mm/s causes the surface von Mises stress to reach 200 Mpa. This reduction in stress is attributed to the laser beam resident duration at a spot. Slow speeds have higher resident times than high speeds. Sufficient resident times allows laser energy to be transmitted into the heating zone. Laser pulsed heating of monocrystalline silicon results in heat absorbtion. Heat absorbtion causes a rise in temperature resulting in thermal expansion of the crystals. A single pulse heating causes expansion and compressive stresses are generated between the crystals. The nanosecond gaps between the laser pulses allows for cooling (due to conduction of heat into the bulk material) to take place. During cooling tensile stresses develop between the crystals and separation of crystals occurs. Increased heating leads to continued crack formation and increased crack population.

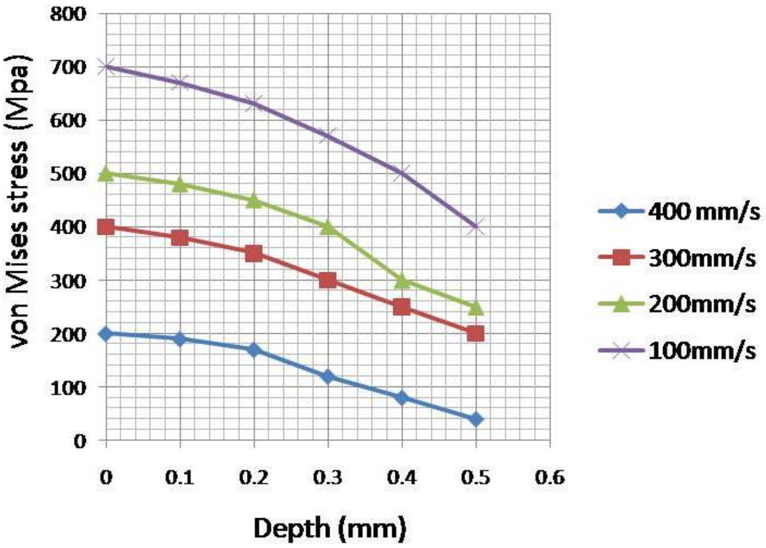

Figure 5.11: The von Mises stress variation along material depth for different laser speeds.

Figure 5.11 shows the stress variation along material depth for different laser speeds. The stress is seen to generally decrease along the depth. Higher values of von Mises stress are seen at the top heating region than the bottom regions. For scan speed of 100 mm/s, the difference between von Mises stress at the top and bottom region is 300 Mpa. The monocrystalline silicon crystals will experience higher microcrack formation at the top region than at the bottom region. This observation is attributed to the heat load being at the top region. The bottom region experiences low heating since since most of heat input to the top region is lost to the ambient through convection. Also, some of the heat from the heating zone is conducted radially into the bulk material.

5.1.2 Effect of spot size

The stationery pulsed laser parameters used for the simulation to determine the effect of spot size on material temperature and thermal stress are listed in Table 5.2.

Table 5.2: Parameters used for the simulation of spot size.

Parameter	**Value**
Laser power	100 W
Pulse width	10 ns
Machining time	1 ms
Wafer thickness	0.5 mm
Scan speed	0 mm/s (stationery)

5.1.2.1 Temperature field analysis

Figure 5.12 shows the surface temperatures of the material for different laser beam spot sizes. Figure 5.13 shows the temperature distribution along the material thickness for the various laser beam spot diameters. Figure 5.14 shows the kerf profiles for the different laser beam spot diameters.

For a beam spot diameter of 0.1 mm (Figures 5.12a and 5.13a), the temperature of the material below the beam spot reaches over 7000 K. The spot size of 0.1 mm delivers a power intensity of 12.7 GW/m^2. The whole thickness of the material below the heating zone is ablated. The zone closest to the heating zone reaches temperatures over 4500 K, which is past silicon boiling point of 3514 K. This zone experiences melting and boiling.

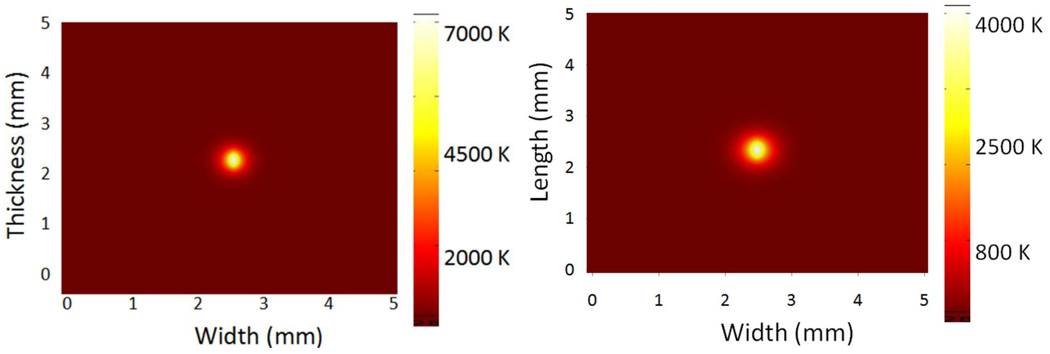

(a) spot diameter=0.1 mm (b) spot diameter=0.4 mm

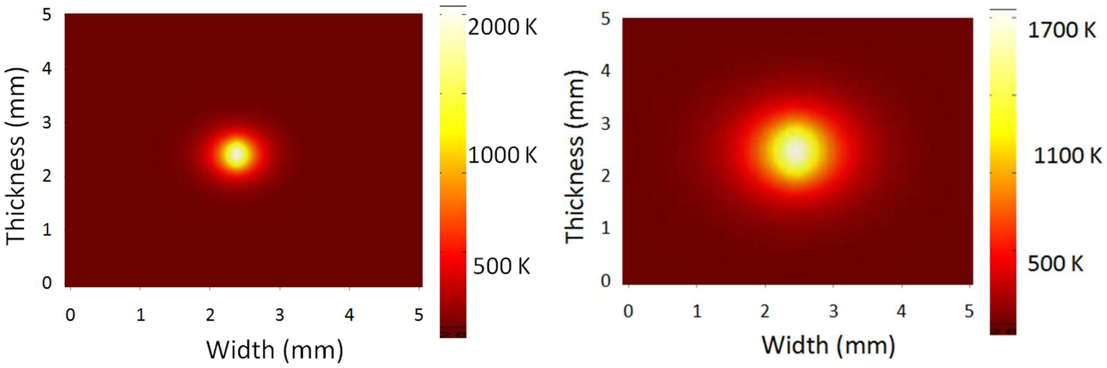

(c) spot diameter=0.7 mm (d) spot diameter=1 mm

Figure 5.12: Surface temperatures of the material for different laser beam spot sizes.

The laser also cuts through the material thickness, as shown in Figure 5.14a. This spot size can be used for microdrilling through monocrystalline silicon. However, this spot size is not optimal for the micromachining of this workpiece, due to the melting caused to the region closest to the heating zone.

For a beam spot diameter of 0.4 mm (Figures 5.12b and 5.13b), the temperature of the material below the beam spot reaches 4000 K. This spot size delivers a power intensity of 795 MW/m^2. The heating zone reaches boiling point and is evaporated. The zone closest to the heating zone reaches temperatures up to 2500 K. This zone experiences melting since the temperatures reached here surpass the silicon melting temperature of 1683 K. The laser cuts through the material thickness, as shown in Figure 5.14b.

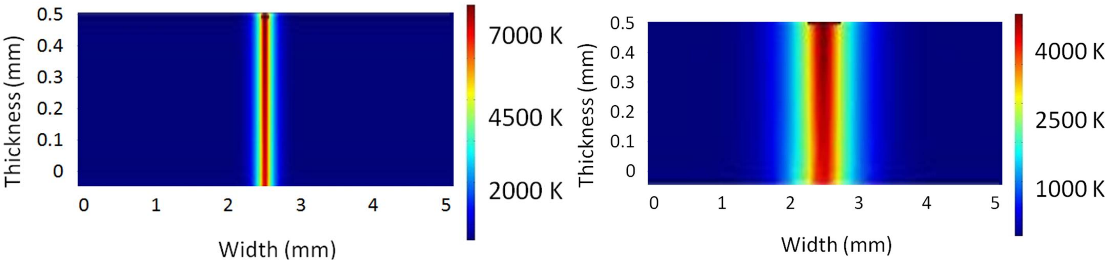

(a) spot diameter=0.1 mm (b) spot diameter=0.4 mm

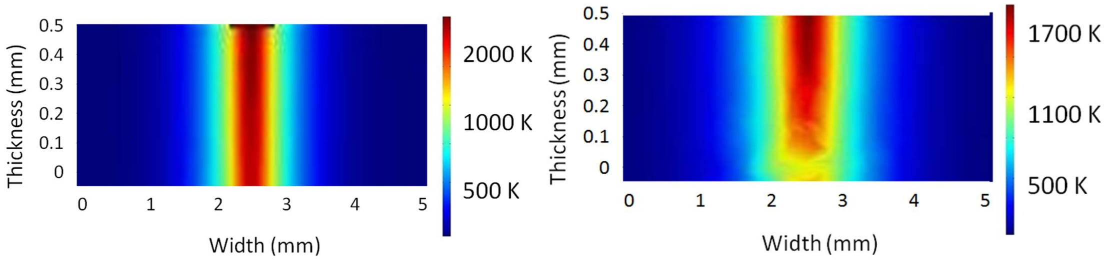

(c) spot diameter=0.7 mm (d) spot diameter=1 mm

Figure 5.13: Temperature distribution along the material thickness for different laser beam spot diameters.

The melting of the region close to the heating zone willnot be as extensive as for the 0.1 mm spot size. The laser cuts through the material thickness, as shown in Figure 5.4b. The minimal melting of the zone closest to the heating zone makes this spot size the optimal choice for micromachining through silicon.

For a beam spot diameter of 0.7 mm (Figures 5.12c and 5.13c), the temperature of the material below the beam spot reaches 2000 K. This spot size delivers a power intensity of 259 MW/m^2. This zone experiences melting since the temperatures reached here surpass the silicon melting temperature of 1683 K. The region closest to the heating zone reaches temperatures up to 1000 K and does not melt. The laser does not cut through material thickness, as shown in Figure 5.14c. For a beam spot diameter of 1 mm (Figures 5.12a and 5.13a), the heating zone temperature reaches 1700 K and experiences melting. This spot size delivers a power intensity of 127 MW/m^2. The other heat affected zones do not reach the melting point. The laser does not cut

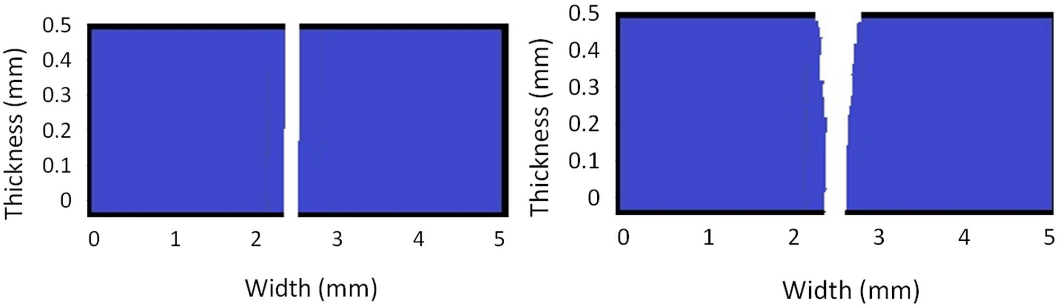

(a) spot diameter=0.1 mm (b) spot diameter=0.4 mm

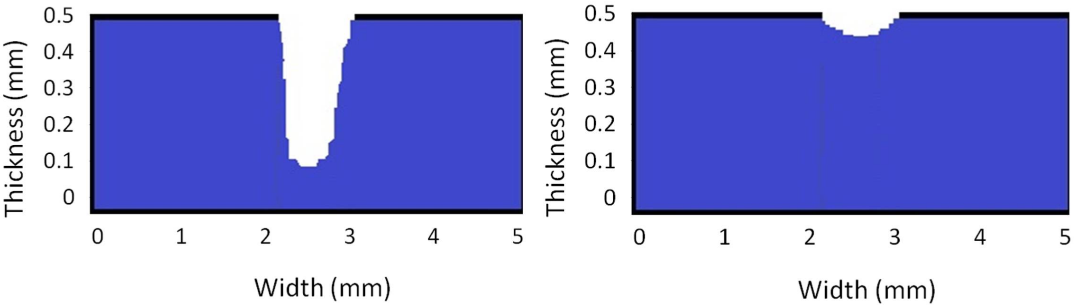

(c) spot diameter=0.7 mm (d) spot diameter=1 mm

Figure 5.14: Kerf profiles for different laser beam spot diameters.

through material thickness, as shown in Figure 5.14d. Both these spot sizes result to the least melting of the regions close to the heating zones. They will both be optimal for micromachining of monocrystalline silicon with minimal HAZ.

Figure 5.15 shows how the material surface temperature at the laser spot compares for various spot sizes. The material temperature at the heating zone is seen to reduce (7000 k to 1800k) as the spot sizes increases from 0.1 mm to 1 mm respectively. The temperature is seen to generally reduce as the spot size increases. This reductions are to be expected since the beam intensity at a spot reduced with increasing diameter. The spot size of 0.1 mm delivers a power intensity of 12.7 GW/m^2 while the spot size of 1 mm delivers a power intensity of 127 MW/m^2.

Figure 5.16 shows the temperature profile along the material depth for different spot

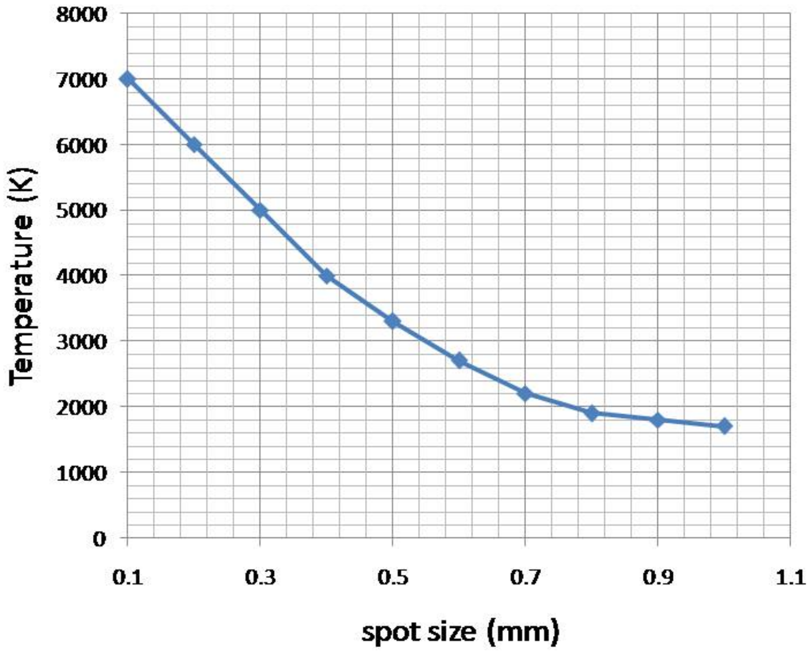

Figure 5.15: Surface temperature at laser spot for different laser spot sizes.

sizes. The temperature is seen to generally reduce through the depth of the work piece. Temperatures of 7000 K and 6000 K are seen at the top and bottom of the workpiece for the 0.1 mm spot size. Temperatures of 6000 K and are seen at the top and bottom of the workpiece for the 1 mm spot size respectively. The temperature difference between the top region and the bottom region results in heat transfer from the region of high temperature (heating zone) to the regions of low temperature. Three mechanisms of heat transfer take place here. First, the top surface of the workpiece experiences convection heat loss to the ambient at 273 K. Second, heat conduction takes place radially in all directions in the workpiece. Lastly, the region directly below the heating zone is semitransparent and is heated up by the the laser light radiation.

Figure 5.17 shows the influence of laser spot size on kerf depth. The kerf depth is seen to generally reduce as the spot size increases. Spot sizes (0.1 mm and 0.4 mm) result in material being drilled through the whole thickness. These spot sizes have high enough

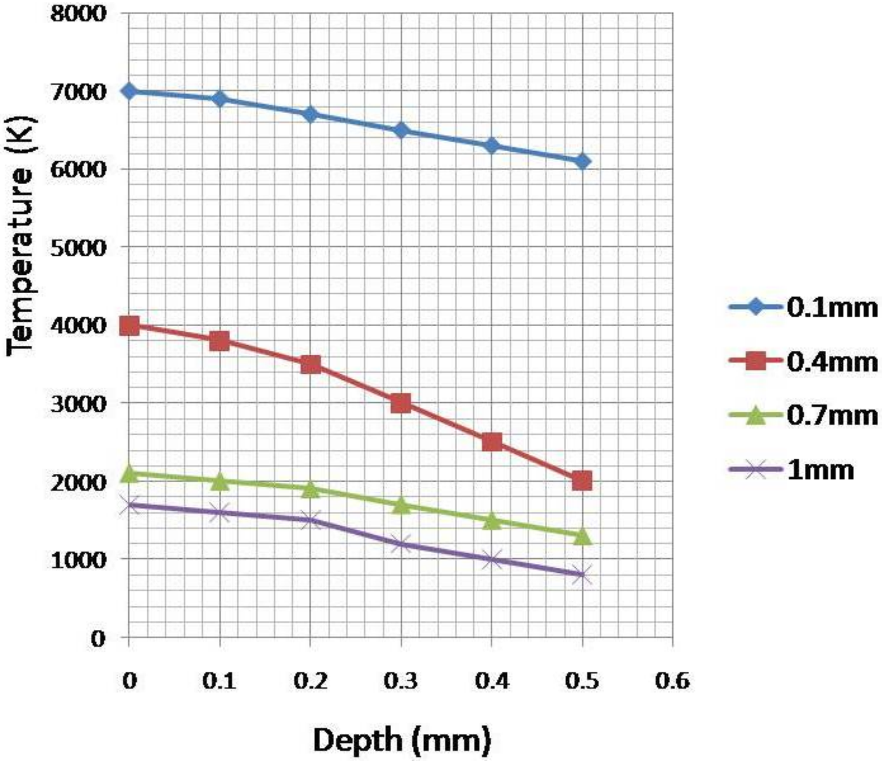

Figure 5.16: Influence of laser spot size on temperature along material depth.

power intensities to heat up the material in a short time and cause melting in the whole region below the heating zone. Spot sizes (0.7 mm and 1 mm) result in shallow drilling with minimal melting of closer regions. The spot size of 0.7 mm results in kerf depth of 0.4 mm. For the spot size of 1 mm, kerf depth of 0.04 mm resulted. The reduction in kerf depth as spot size increases is attributed to the reduction in the beam intensity as a spot increased in diameter. The spot size of 0.1 mm delivers a power intensity of 12.7 GW/m^2 while the spot size of 1 mm delivers a power intensity of 0.127 GW/m^2.

5.1.2.2 Stress field analysis

Figure 5.18 shows the surface von Mises stress fields for different laser beam spot diameters. Figure 5.19 shows the von Mises stress distribution along material thickness

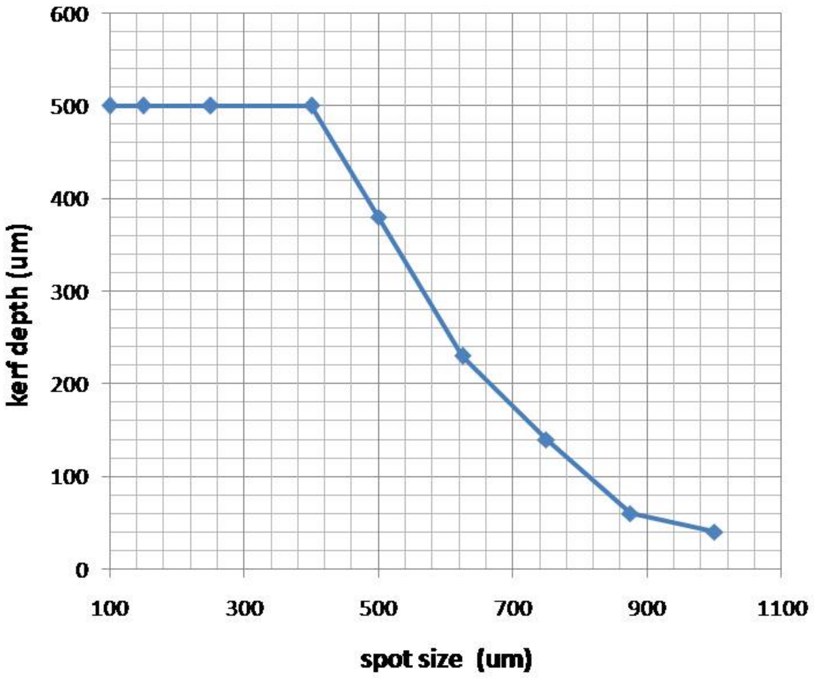

Figure 5.17: Influence of laser spot size on kerf depth.

for different laser beam spot diameters. Figure 5.20 shows the extent of microcracks formation along material thickness for different spot sizes. von Mises stress yield criterion is used for stress analysis. When the maximum von Mises stress exceeds the fracture (yield) stress of silicon, 300 Mpa, microcracks are formed.

At the spot size of 0.1 mm (Figures 5.18a and 5.19a), stress at the heating zone reaches 900 Mpa. The zone closest to the heating zone reaches 500 Mpa. These two zones experience crack formation, since their stresses have exceeded the fracture (yield) stress of silicon (300 Mpa). The stress at the zone farthest from the heating zone reaches 100 Mpa. Cracks will not be initiated in this far zone, as shown in Figure 5.20a. This laser spot size is not optimal for micromachining monocrystalline silicon since the a spot size will result to high thermal stresses within the material and microcrack formation.

At the spot size of 0.4 mm (Figures 5.18b and 5.19b), stress at the heating zone reaches

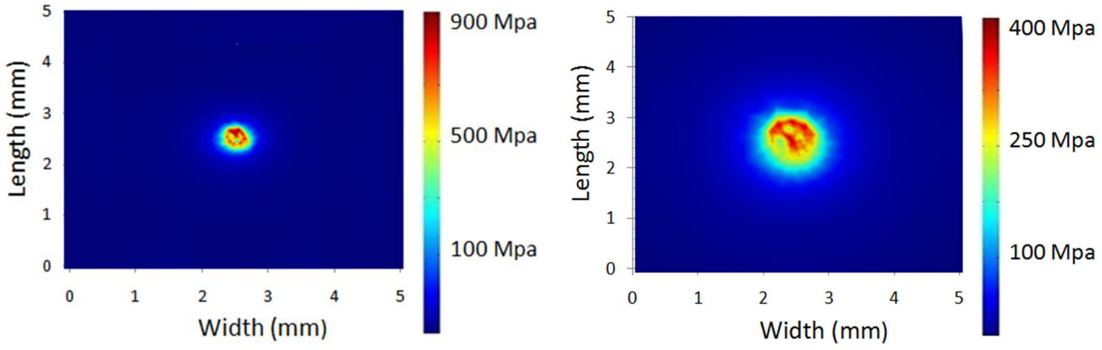

(a) spot diameter=0.1 mm (b) spot diameter=0.4 mm

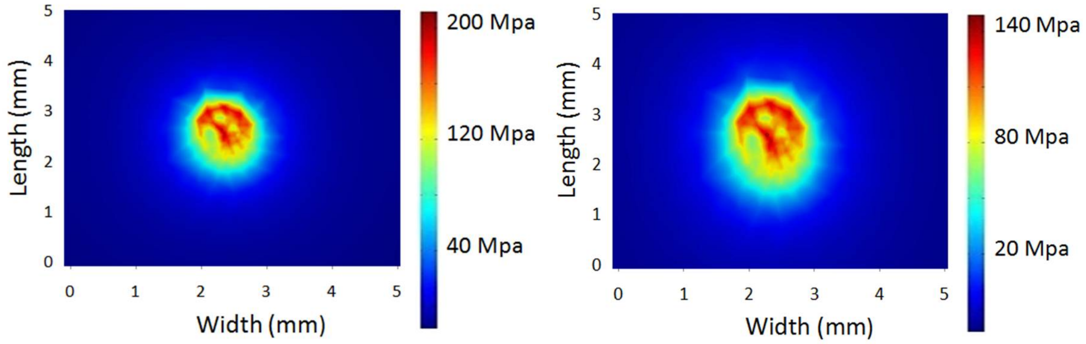

(c) spot diameter=0.7 mm (d) spot diameter=1 mm

Figure 5.18: Surface von Mises stress fields for different laser beam spot diameters.

400 Mpa. There is crack formation in this zones since the stress has exceeded 300 Mpa. The stress at the zone closest to the heating zone reaches 250 Mpa. The stress at the zone farthest from the heating zone reaches 100 Mpa. Cracks will not be initiated in this zones, as shown in Figure 5.20b. This spot size is not optimal for micromachining monocrystalline silicon. The spot size willresult in thermal stresses within the material and microcrack formation. Though, 0.4 mm spot size is a better choice than 0.1 mm spot size, since it will result to less microcracking during laser micromachining.

At the spot size of 0.7 mm (Figures 5.18c and 5.19c), stress at the heating zone reaches 200 Mpa. There is no crack formation in this zones since the stress has not exceeded 300 Mpa. The stress at the zone closest to the heating zone reaches 120 Mpa. The

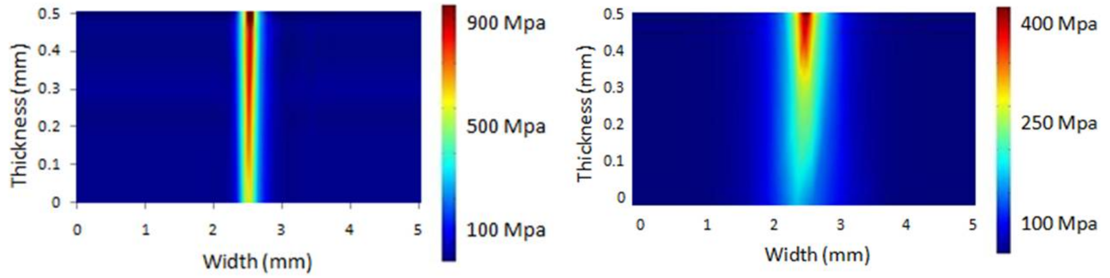

(a) spot diameter=0.1 mm (b) spot diameter=0.4 mm

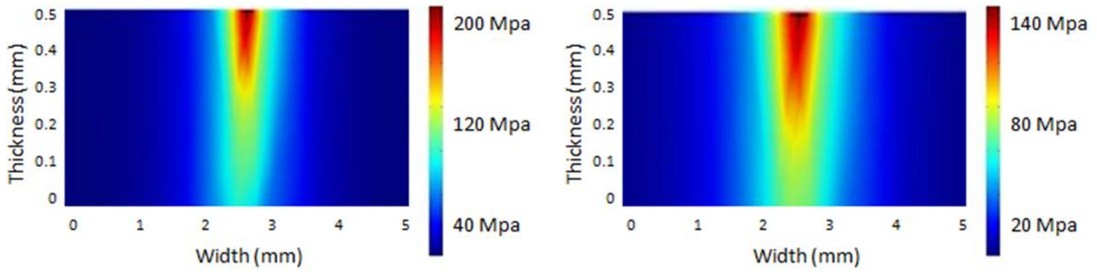

(c) spot diameter=0.7 mm (d) spot diameter=1 mm

Figure 5.19: von Mises stress distribution along material thickness for different laser beam spot diameters.

stress at the zone farthest from the heating zone reaches 40 Mpa. Cracks is not initiated in these three zones, as shown in Figure 5.20c.

At the spot size of 1 mm (Figures 5.18d and 5.19d), stress at the heating zone reaches 140 Mpa. There is no crack formation in this zones since the stress has not exceeded 300 Mpa. The stress at the zone closest to the heating zone reaches 80 Mpa. The stress at the zone farthest from the heating zone reaches 20 Mpa. Cracks is not initiated in these three zones, as shown in Figure 5.20d. Both the spot sizes(0.7 mm and 1 mm) are optimal for machining since they will not contribute to thermal stresses sufficiently high to cause crack formation in the material.

Figure 5.21 shows how the von Mises stress at the laser spot on the material varies with spot sizes. The 0.1 mm spot size results in the most microcracking while the 1 mm spot size results in the least microcracking. The spot size of 0.1 mm causes the surface

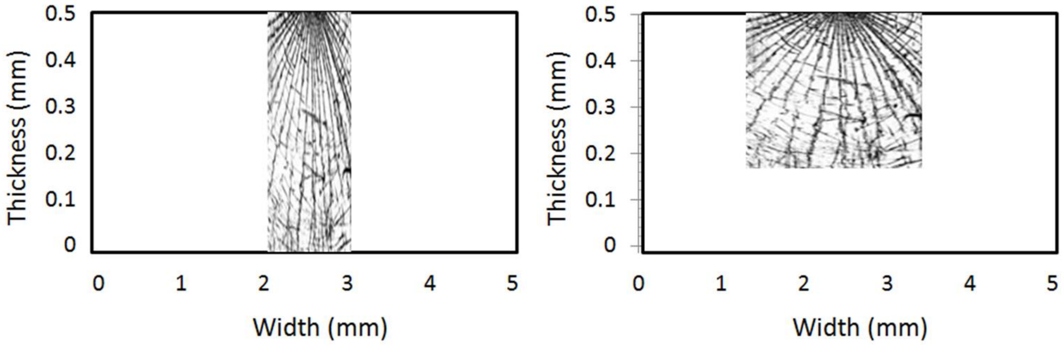

(a) spot diameter=0.1 mm (b) spot diameter=0.4 mm

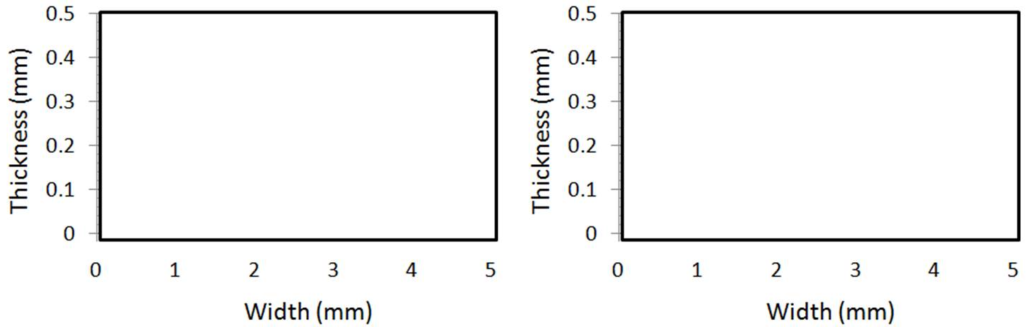

(c) spot diameter=0.7 mm (d) spot diameter=1 mm

Figure 5.20: Extent of microcracks formation along material thickness for different spot sizes.

von Mises stress of 900 Mpa. The spot size of 1 mm causes the surface von Mises stress to reach 120 Mpa. The von Mises stress is seen to reduce as the spot size increases. This reduction in stress is attributed to the laser beam decrease in power intensity as the beam spot size increases. The spot size of 0.1 mm has a power intensity 100 times larger than the 0.1 mm spot size for the same power.

Figure 5.22 shows the stress variation along material thickness for different spot sizes. The stress is seen to generally decrease along the depth. Higher values of von Mises stress are seen at the top heating zone than at the bottom regions. For instance, for the spot size of 0.1 mm, the difference between von Mises stress at the top and bottom region is 400 Mpa. The monocrystalline silicon crystals will experience higher

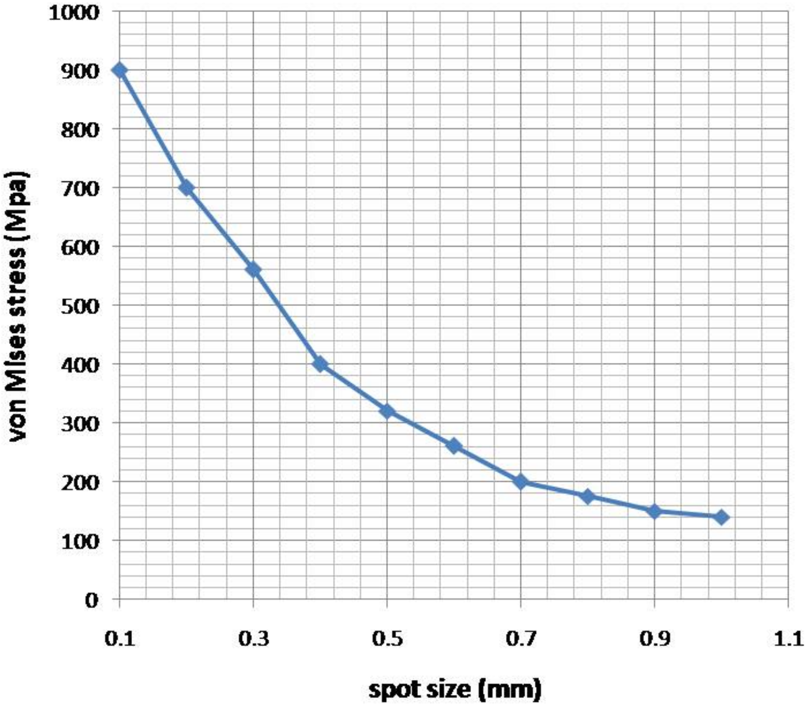

Figure 5.21: Influence of laser spot size von Mises stress on the material surface.

microcrack formation at the top region than at the bottom region. This observation is attributed to the heat load being at the top region. The bottom region experiences low heating since since most of heat input to the top region is lost to the ambient through convection. Also, some of the heat from the heating zone is conducted radially into the bulk material.

5.1.3 Effect of power

The stationery pulsed laser parameters used for the simulation to determine the effect of power on material temperature and thermal stress are listed in Table 5.3.

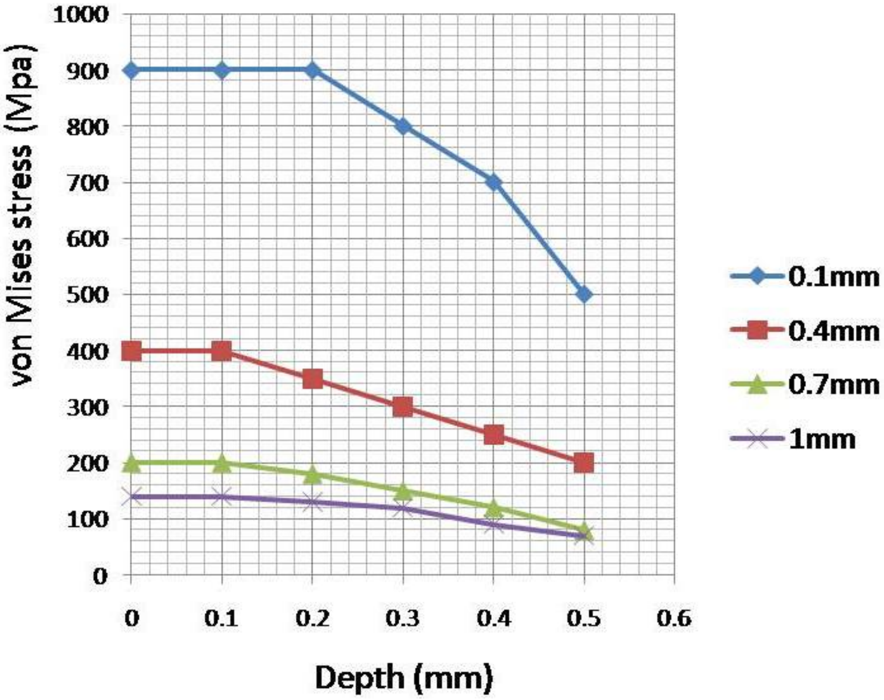

Figure 5.22: Stress variation along material thickness for different spot sizes.

Table 5.3: Parameters used for the simulation of power.

Parameter	**Value**
Pulse width	10 ns
Spot diameter	0.4 mm
Machining time	1 ms
Scan speed	0 mm/s (stationery)

5.1.3.1 Temperature field analysis

Figure 5.23 shows the surface temperatures field of the material for different laser beam power. Figure 5.24 shows the temperature distribution along the material thickness for the various laser beam power. Figure 5.25 shows the kerf profile predictions along the material thickness for the various laser beam power.

For a power of 50 W (Figures 5.23a and 5.24a), the temperature of the heating zone reaches 2200 K. This power delivers a power intensity of 397 MW/m^2. The heating

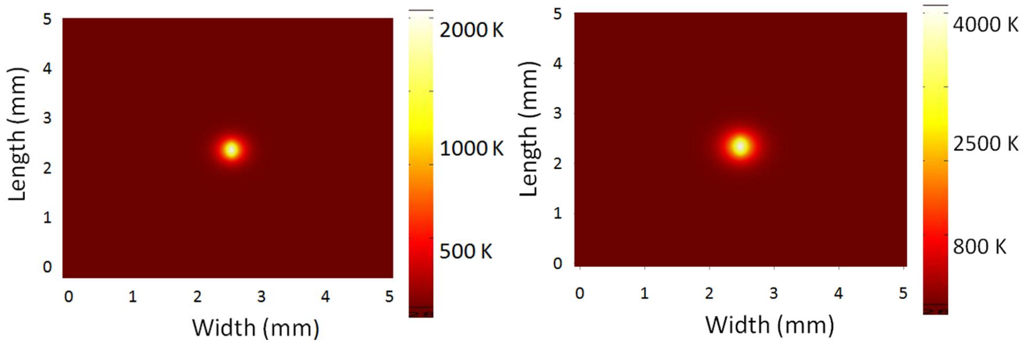

(a) power=50 W (b) power=100 W

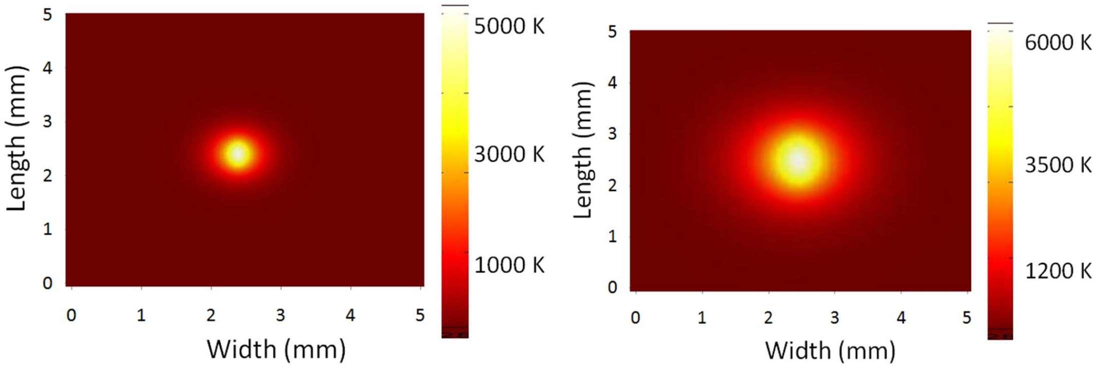

(c) power=125 W (d) power=150 W

Figure 5.23: Surface temperatures of the material for different laser beam power.

zone reaches melting point but does not reach boiling point. The zone closest to the heating zone reaches temperatures up to 1100 K. This zone does not melt since the temperatures reached here are below the silicon melting temperature of 1683 K. The laser does not cut through material thickness as shown in Figure 5.25a. This power results to the least melting of the region closest to the heating zone. 50 W power is optimal for micromachining of monocrystalline silicon with minimal HAZ, in an application such as microscribing.

For a power of 100 W (Figures 5.23b and 5.24b), the temperature of the material below the beam spot reaches 4000 K. This power delivers a power intensity of 795 MW/m^2. The heating zone reaches boiling point and is partially ablated. The zone close to the

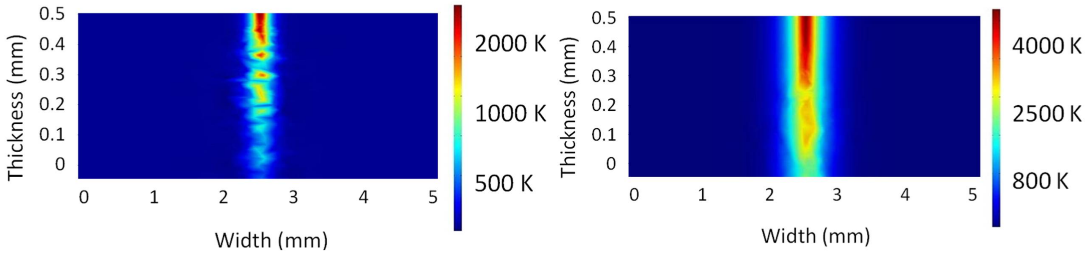

(a) power=50 W

(b) power=100 W

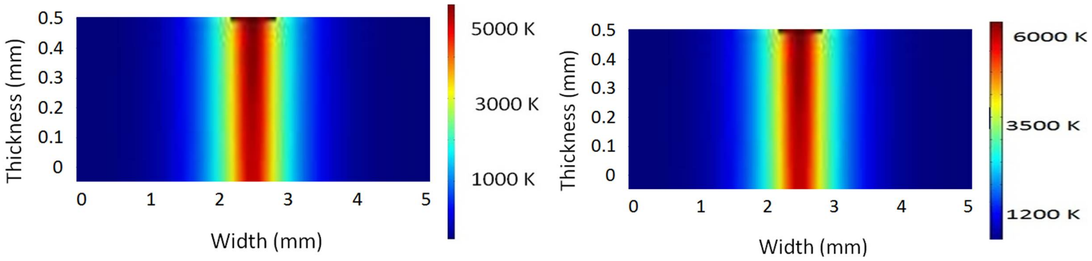

(c) power=125 W

(d) power=150 W

Figure 5.24: Temperature distribution along the material thickness for different laser beam power.

heating zone reaches temperatures up to 2000 K. The laser does not drill fully through the material thickness as shown in Figure 5.25b. This power results to the some melting of the region closest to the heating zone and will result to extensive HAZ than the 50 W power.

For a power of 125 W (Figures 5.23c and 5.24c), the temperature of the material below the beam spot reaches 5000 K. This power delivers a power intensity of 994 MW/m^2. The heating zone reaches boiling point and is partially ablated. The zone close to the heating zone reaches temperatures of 2500 K. This zone therefore experiences melting since the temperatures reached here surpass the silicon melting temperature of 1683 K. The laser also cuts through the material thickness, as shown in Figure 5.25c. The melting of the region close to the heating zone is not as extensive as for the 150 W power. Therefore the HAZ is minimal. The laser cuts through the material thickness, as shown in Figure 5.4b. This power is the optimal choice for micromachining through

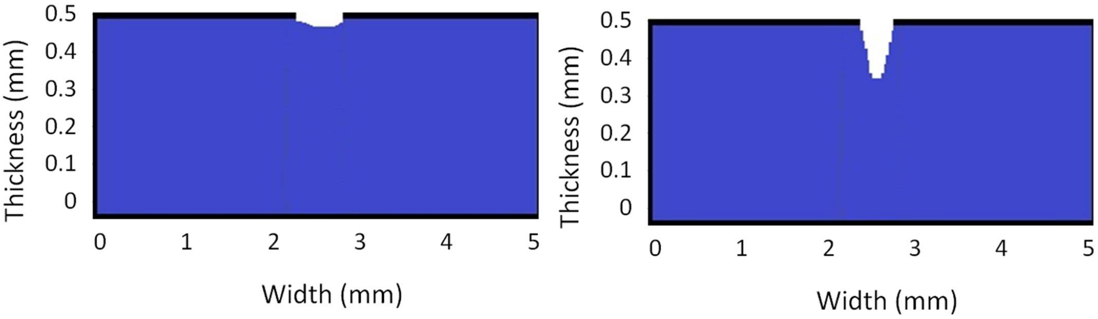

(a) power=50 W (b) power=100 W

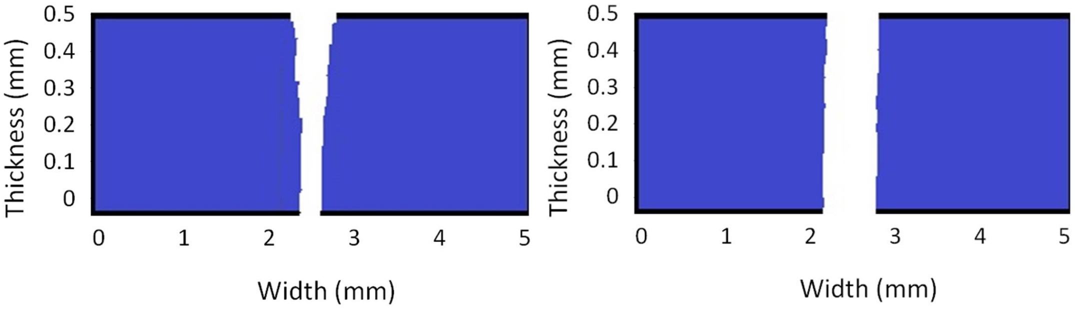

(c) power=125 W (d) power=150 W

Figure 5.25: Kerf profile predictions for different laser beam power.

silicon.

For a power of 150 W (Figure 5.23d and 5.24d), the theoretical temperature of the material below the beam spot reaches over 6000 K. This power delivers a power intensity of 1193 MW/m^2. The whole thickness of the material at the heating zone is totally ablated. The zone closest to the heating zone reaches temperatures over 3500 K which is past silicon boiling point of 3514 K. The laser cuts through the material thickness, as shown in Figure 5.25d. This laser power is useful for drilling and cutting through silicon by ablation but will result to extensive HAZ than using the 125 W power.

Figure 5.26 show the surface temperature at the laser spot for different laser power. The temperature is seen to generally increase as the power increases. This increments are to be expected since the beam spot size was constant, while the beam intensity at a

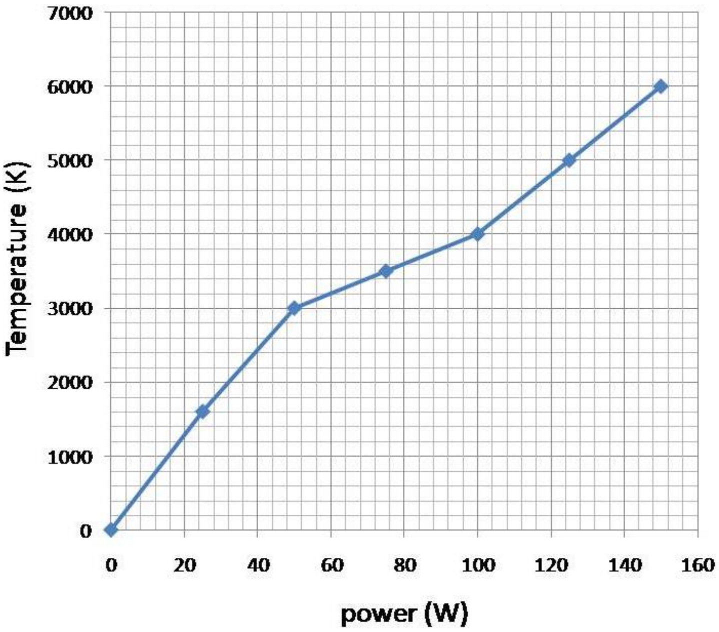

Figure 5.26: Surface temperature at laser spot for different laser power.

spot increased with increasing power. A power intensity of 397 MW/m^2 was delivered by the 50 W power, while a power intensity of 1193 MW/m^2 was delivered by the 150 W power. The 150 W power caused surface temperature of 6000 W, while the 50 W power caused a surface temperature of 2000W. High power implies a fast energy delivery per unit time. This will in turn cause a fast rise in temperature.

Figure 5.27 shows the temperature profile along the material depth for different powers. The temperature is seen to generally reduce through the depth of the work piece. This reduction is to be expected since heat conduction takes place in the material. The mean temperature drop between between the top surface and the bottom surface of the workpiece is 1500 K for all the four scan speeds. The temperature difference results in heat transfer from the region of high temperature (heating zone) to the regions of low temperature. Three mechanisms of heat transfer take place here. First, the top surface of the workpiece experiences convection heat loss to the ambient at 273 K. Second, heat conduction takes place radially in all directions in the workpiece. Lastly,

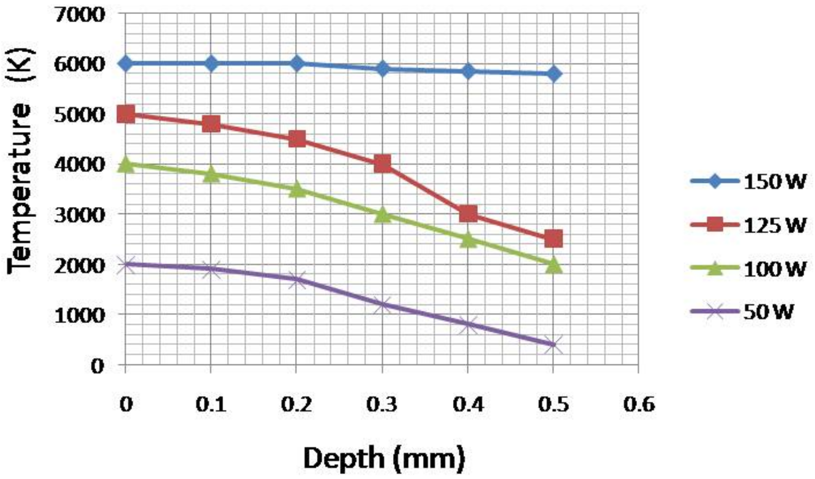

Figure 5.27: Temperature variation along depth of material for different laser power.

the region directly below the heating zone is semitransparent and is heated up by the the laser light radiation.

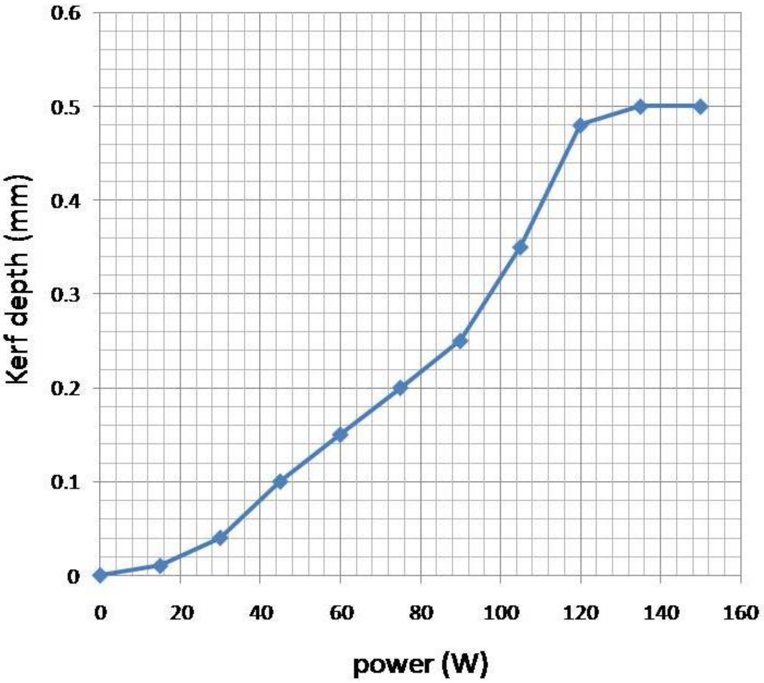

Figure 5.28: Influence of laser power on kerf depth.

Figure 5.28 shows the influence of laser power on kerf depth. The kerf depth is seen to generally increase as the power increases. The power (125 W and 150 W) result in material being drilled through the whole thickness. These laser powers have high enough power intensities (994 MW/m^2 and 1193 MW/m^2 respectively)to heat up the material in a short time and cause melting in the whole region below the heating zone. The laser powers (50 W and 100 W) result in shallow drilling with minimal melting of closer regions. The increase in kerf depth as power increases is attributed to the in the beam intensity. The power of 50 W delivers a power intensity of 397 MW/m^2 while the 150 W power of delivers a power intensity of 1193 MW/m^2.

5.1.3.2 Stress field analysis

Figure 5.29 shows the surface von Mises stress fields for different laser beam power. Figure 5.30 shows the von Mises stress distribution along material thickness for different laser beam power. Figure 5.31 shows the extent of microcracks formation along material thickness for different laser beam power. von Mises stress yield criterion is used for stress analysis. When the maximum von mises stress exceeds the fracture (yield) stress of silicon, 300 Mpa, microcracks are initiated and propagated.

At the power of 150 W (Figures 5.29d and 5.30d), stress at the heating zone reaches 650 Mpa. The zone closest to the heating zone reaches 400 Mpa. These two zones experience crack formation, since their stresses have exceeded 300 Mpa. The stress at the zone farthest from the heating zone reaches 200 Mpa. Cracks is not initiated in this zone, as shown in Figure 5.31d. This laser power willnot be optimal for micromachining monocrystalline silicon since this power will result to high thermal stresses within the material and microcrack formation.

At the power of 125W (Figures 5.29c and 5.30c), stress at the heating zone reaches 500 Mpa. The stress at the zone closest to the heating zone reaches 300 Mpa. These

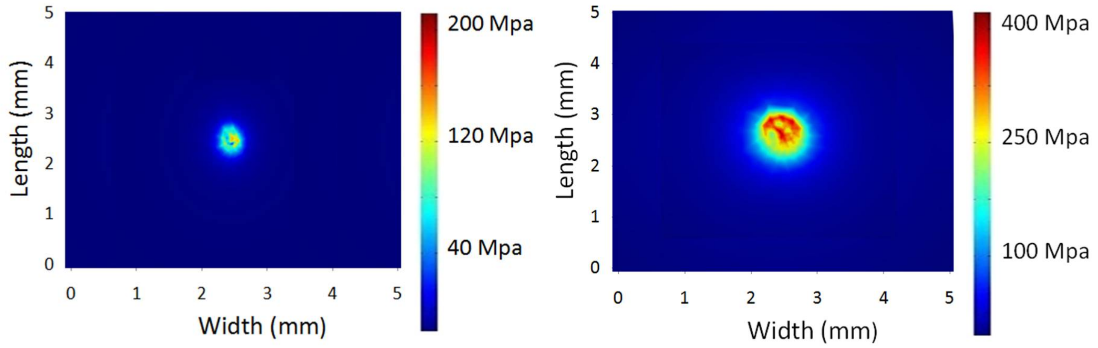

(a) power=50 W (b) power=100 W

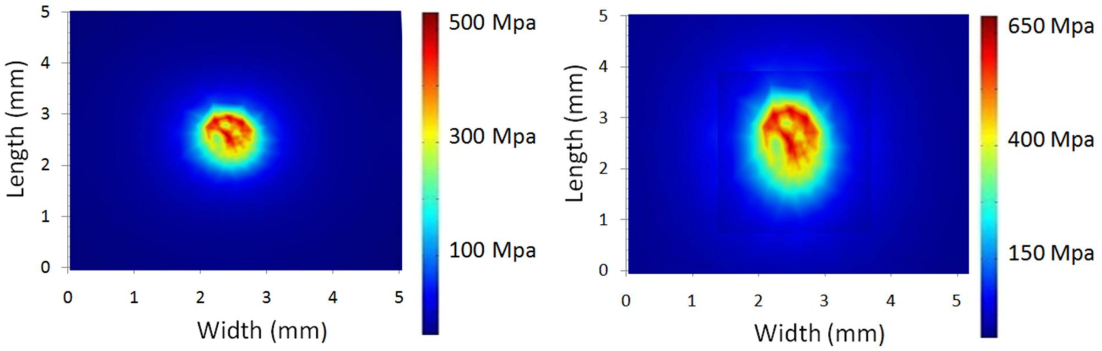

(c) power=125 W (d) power=150 W

Figure 5.29: Surface von Mises stress fields for different laser beam power.

two zones experience crack formation, since their stresses have exceeded 300 Mpa. The stress at the zone farthest from the heating zone reaches 100 Mpa. Cracks is not initiated in this zone, as shown in Figure 5.31c. This laser power is not optimal for micromachining monocrystalline silicon. This power will result in thermal stresses within the material and microcrack formation. Though, 125 W is a better choice than 150 W, since it will result to less microcracking during laser micromachining.

At the power of 100 W (Figures 5.29b and 5.30b), stress at the heating zone reaches 400 Mpa. There is crack formation in this zones since the stress has exceeded 300 Mpa. The stress at the zone closest to the heating zone reaches 250 Mpa. The stress at the zone farthest from the heating zone reaches 100 Mpa. Cracks is not initiated

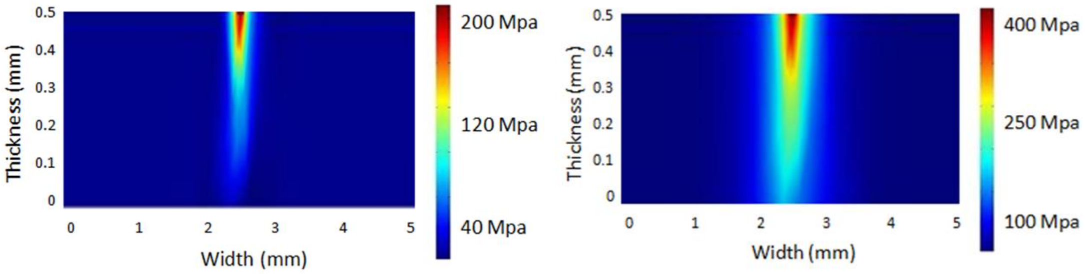

(a) power=50 W (b) power=100 W

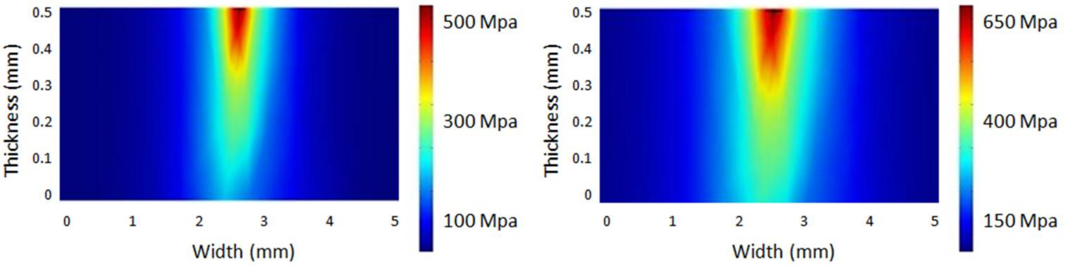

(c) power=125 W (d) power=150 W

Figure 5.30: von Mises stress distribution along material thickness for different laser beam power.

in these two latter zones, as shown in Figure 5.31b This laser power is not optimal for micromachining monocrystalline silicon. Such power will result in thermal stresses around the heating zone and microcrack formation. The power of 100W is a better choice than 150 W and 125 W, since it will result to less microcracking during laser micromachining.

At the power of 50 W (Figures 5.29a and 5.30a), stress at the heating zone reaches 200 Mpa. There is no crack formation in this zones since the stress has not exceeded 300 Mpa. The stress at the zone closest to the heating zone reaches 120 Mpa. The stress at the zone farthest from the heating zone reaches 40 Mpa. Cracks is not initiated in all these zones, as shown in Figure 5.31a. This laser power is optimal for micromachining monocrystalline silicon. This power will not result in thermal stresses around the heating zone and hence no microcrack formation. The power of 50W is the optimal

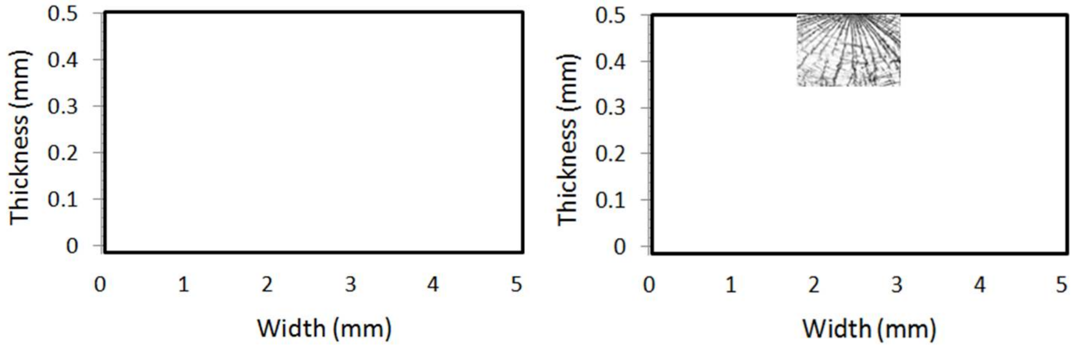

(a) power=50W (b) power=100W

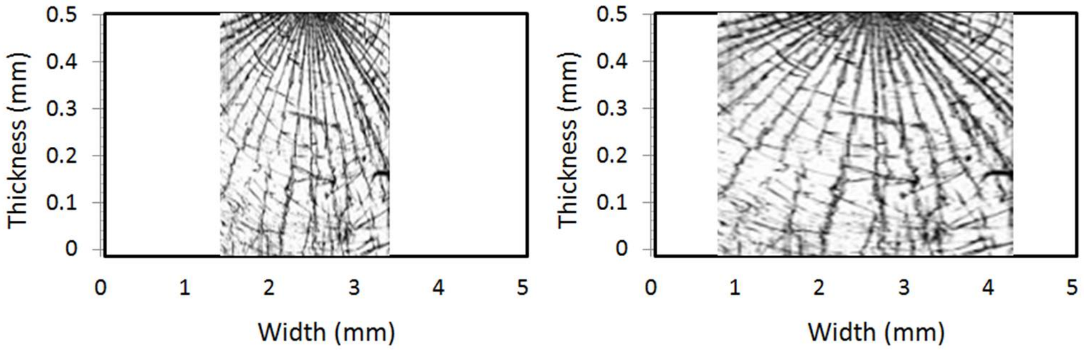

(c) power=125W (d) power=150W

Figure 5.31: Extent of microcracks formation along material thickness for different laser beam power.

choice since it will result to zero microcracking during laser micromachining.

Figure 5.32 shows how the maximum von Mises stress at the laser spot on the material surface varies with power. The stress is seen to generally increase as the power increases.

Figure 5.33 shows the stress variation along material depth for different laser powers. Higher values of von Mises stress are seen at the top heating zone than at the bottom regions. For instance, for the power of 150 W, the difference between von Mises stress at the top and bottom region is 300 Mpa. The monocrystalline silicon crystals will experience higher microcrack formation at the top region than at the bottom region. This observation is attributed to the heat load being at the top region. The bottom region experiences low heating since since most of heat input to the top region is lost

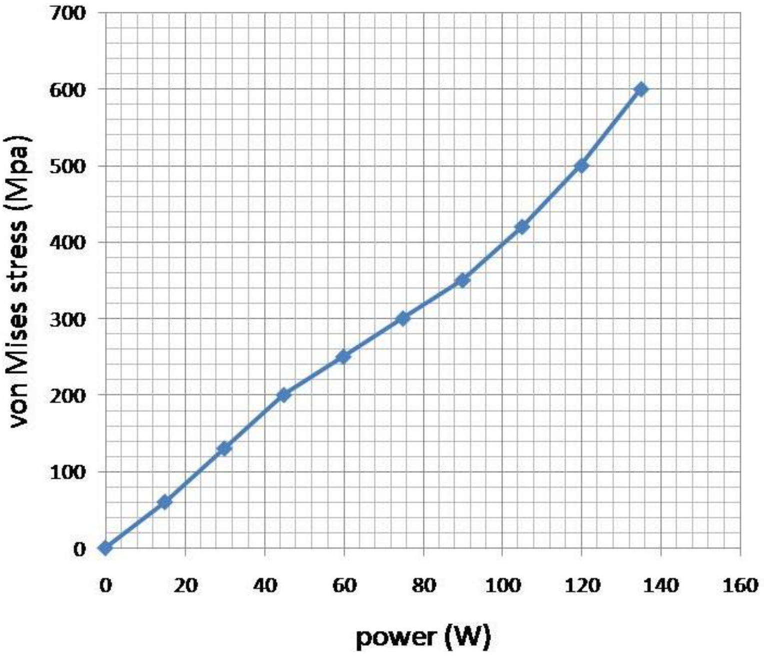

Figure 5.32: Influence of laser power on stress on the material surface.

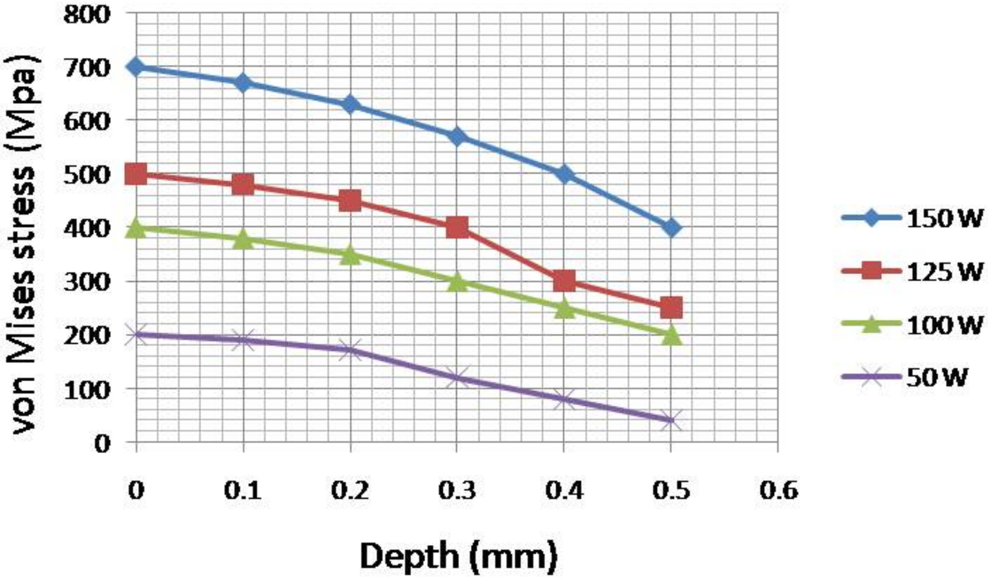

Figure 5.33: Stress variation along material depth for different laser powers.

to the ambient through convection. Also, some of the heat from the heating zone is conducted radially into the bulk material.

5.2 Validation of results

5.2.1 Effect of laser scan speed on kerf depth

Experiments on the laser scan speed effect in nanosecond laser machining of silicon were performed by Yasa and Kruth [57]. Comparison is made for the simulated kerf depths with experimental ones reported by Yasa and Kruth [57], as shown in Figure 5.34. In both cases, it can generally be seen that kerf depths reduced with an increase in scan speeds. From simulation, 100 mm/s scan speed resulted in 50 um kerf depth, while for experimental, 100 mm/s scan speed resulted in 45 um kerf depth. From simulation, 600 mm/s scan speed resulted in 8 um kerf depth, while for experimental, 100 mm/s scan speed resulted in 10 um kerf depth. As the scan speed increases the energy per unit area decreases. The scan speed also influences the overlapping between subsequent laser pulses, the slower the speed the greater the overlap. Both tests were carried out under the same conditions except the experimental one was carried out under regular air. The average depth of cut for the scan speeds is close. Hence the influence of air was negligibe.

The simulation depth of cut for the 100 mm/s scan speed was deeper than for the experimental by 5 um. This could be attributed to external variables not considered in the model, such as the plume/vapor screening effect of laser micromachining. The vapor attenuates the intensity of incident laser radiation. There is high vapor production for the slow scan speed machining. For high laser scan speeds, the laser fluence on the surface of the silicon is less than the time for plasma formation rate.

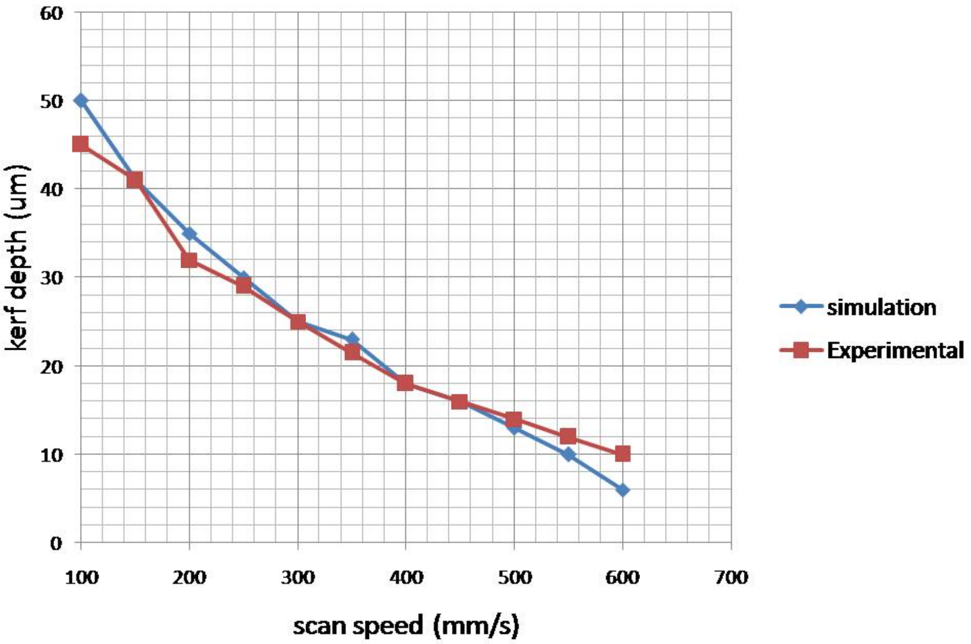

Figure 5.34: Influence of laser scan speed on resulting kerf depth in material.

5.2.2 Effect of laser spot diameter on temperature

Comparison is made for the simulated temperature with experimental ones reported by Yang et al. [58], as shown in Figure 5.35. These show the values for the surface temperature versus spot sizes. Spot sizes of 0.1 mm cause surface temperature of 6000 K and 7000 K for the experimental and the simulation cases, respectively. Spot sizes of 1 mm cause surface temperature of 1300 K and 1800 K for the experimental and the simulation cases, respectively. In both cases, the temperature is seen to generally reduce as the spot size increases. The graphs display concavity. The gradients steepens as the spot sizes reduce. This is attributed to the to the non linear relationship between the power intensity and the spot diameter. The power intensity varies inversely with the square of the spot diameter. The slope tangents of both graphs are close. Since the experiments were conducted in air, possible effects of surface defects such as the native oxide coating were considered to affect the results. The native oxide coating

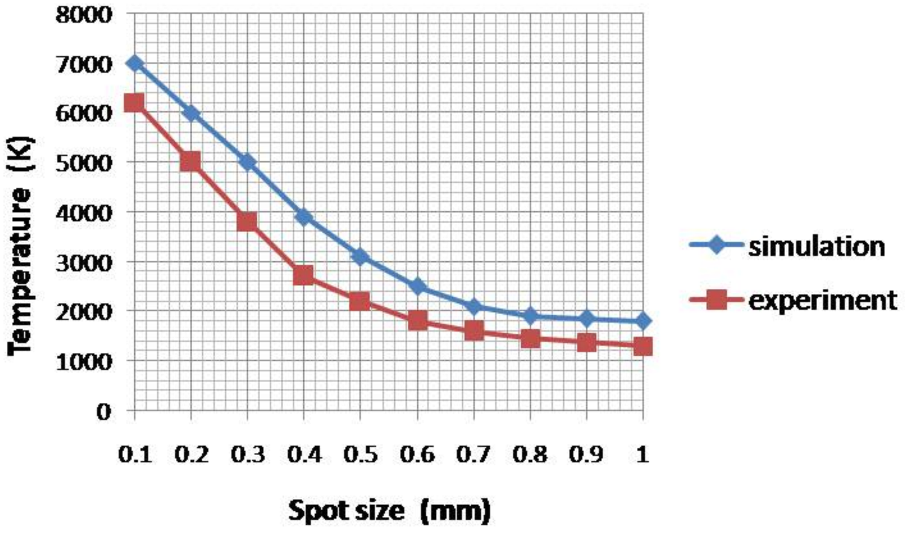

Figure 5.35: Influence of laser spot sizes on surface temperature of material.

forms when monocrystalline silicon is exposed to air. This coating is opaque to laser light and prevents some light from reaching the bulk material. This explains why the experimental workpiece attained lower temperatures than the simulation ones.

5.2.3 Effect of laser power on kerf depth

Experiments on the laser power effect in nanosecond laser machining of silicon were performed by Yasa and Kruth [57], as shown in Figure 5.36. Comparison is made for the simulated kerf depths with experimental ones reported by Yasa and Kruth [57]. Both graphs have positive gradients. In both cases, it can generally be seen that kerf depths increased with an increase in power. The gradient for the simulation curve (1.33) is twice the one for experiments (0.66). At the power of 30 W, the simulation kerf depth is 40 um, while the experimental kerf depth is 20 um.

In experimental machining, external variables, such as deposition of molten material into the machined hole, can reduce the expected kerf depth. Also, high power causes

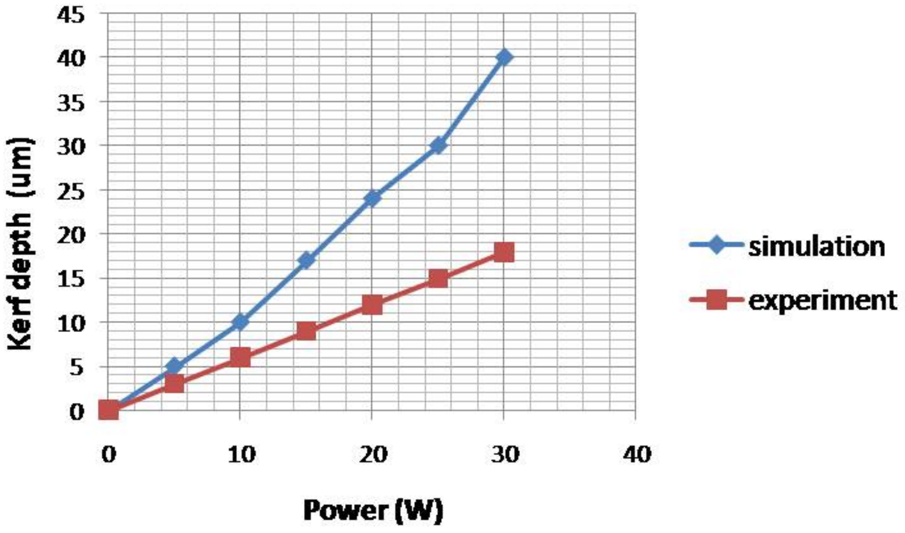

Figure 5.36: Influence of laser power on material kerf depth.

evaporation which result to plume formation. The plume blocks the incoming light from reaching the target. Less power is delivered to workpiece than was expected and less material is removed.

5.3 Summary

In this chapter, the results from simulations investigating the effect of scan speed, spot size and power on the kerf depth and microcracking of monocrystalline silicon have been presented and discussed. These simulation results have been validated by comparison to experimental results. The models satisfactorily predicted the expected kerf depth and microcracking for the various parameters studied.

CHAPTER SIX

6.0 RESULTS

In this study, the effects of laser micromachining parameters i.e., scan speed, beam spot diameter and laser power on the kerf depth and microcrack formation were successfully investigated. A model for predicting the optimal laser beam and laser process parameters for quality machining of silicon wafers was successfully developed. The thermal stress fields and temperature distribution were evaluated successfully using Finite Element Method. The mathematical equations for the simulation model were successfully coded in the $COMSOL^R$ software and the result images analyzed using $IMAGEJ^R$ software.

The relationship between the various laser machining parameters and the output attributes need to be established so that they can be controlled during laser micromachining of monocrystalline silicon to attain desirable outcomes. From the foregoing discussion of the results, the following conclusions were deduced:

1. Microcrack formation: It is desirable to obtain laser beam and process parameters parameters that could result in the least microcrack formation. Microcrack formation results when thermal stresses caused by laser heating exceeds the monocrystalline silicon fracture (yield) limit of 300 Mpa. The laser parameters that yield optimal results for the least microcrack formation are: a scan speed of 400 mm/s, spot size of 1 mm and power of 50W
2. Heat affected Zone. It is desirable to determine optimal laser beam and process parameters that could result to minimal heat affected zone. Extensive heating causes heat affected zones such as melt affected zones and this can result to undesirable cut profiles. It is desirable to select parameters that result to heating

and melting of the desired heating zone only. The laser parameters that yield optimal results for the least melt affected zone are: a scan speed of 400 mm/s, spot size of 1 mm and power of 50W

3. Kerf depths: It is desirable to select optimal laser machining parameters that could result in machining of the desired depth with minimal distortion to work piece. When microdrilling through holes in workpiece. the laser parameters that yield optimal results for the least melt affected zone are: a scan speed of 200 mm/s, spot size of 0.4 mm and power of 125W. For microscribing operation, the laser parameters that yield optimal results for the least melt affected zone are: a scan speed of 400 mm/s, spot size of 1 mm and power of 50W.

4. Scan speeds: Selecting the optimal scan speed which results in the least melt affected zone and least thermal stress is crucial. The scan speed of 400 mm/s is optimal as it results in the least melt affected zone and microcrack formation.

5. Spot size: Selecting the optimal spot size which result in the least melt affected zone and thermal stress is crucial. The spot size of 1 mm results in the least melt affected zone and microcrack formation.

6. Power: Selecting the optimal power which result in the least melt affected zone and thermal stress is crucial. The scan speed of 400 mm/s results in the least melt affected zone and Microcrack formation.

These simulation results were validated by comparison to experimental ones. The models satisfactorily predicted the expected kerf depth and microcrack formation for the laser parameters studied.

CHAPTER SEVEN

7.0 RECOMMENDATIONS

The following are areas in the investigation of the effects of the laser micromachining parameters on the cut quality attributes of monocrystalline silicon that could be further addressed to improve the model.

1. Perform extensive experimental tests in order to better characterise the models developed. The experiments should be carried out in a wide variety of conditions. These conditions can then be included to improve the model. For example, effects of air reaction with monocrystalline silicon during laser heating can be modeled and validated by experiments. Plume/vapor screening effect of laser drilling which was not included in the laser drilling model should be investigated. The effects of assist gas on the laser drilling process were also not considered in the model. These include the cooling effect, and exothermic and oxidation reactions. These should therefore be investigated since they have a great influence on the micromachined quality attributes.

2. The effect of light reflection and radiation on the monocrystalline silicon surface should be considered. Monocrystalline silicon is not completely isotropic. Scattering of light during transmission within the medium may cause the loss of intensity of the laser. Existing mathematical models have not explicitly captured the light scattering phenomenon. An improved model should capture the crystal orientations and how this could affect light transmission, and the effect on temperature distribution within silicon.

3. The effect of change in material properties after the brittle to ductile transition could be included so as to make the model more accurate. Molten monocrystalline

silicon changes from semitransparent to opaque and this should be considered to improve the model. Also, the effects of non-linear temperature distribution in the solid, starting from the solid-liquid interface to the thermal diffusion depth should be included and investigated.

4. A computational fluid dynamics model could be incorporated into the model to facilitate analysis of behaviour of material during melting, flowing, boiling and evaporation. This research modeled only the heat transfer and thermal stress effects. Implementation of the fluid modeling in combination with the heat transfer and thermal stress module will be facilitated by later releases of $COMSOL^R$ software. This would help better characterize the heat affected zones.

REFERENCES

[1] Luo S. and Wang Z., "Studies of chipping mechanisms for dicing silicon wafers," *Journal of Advanced Manufacturing Technology*, vol. 35, pp. 1206–1218, 2008.

[2] Paydenkar C., Poddar A., Chandra H., and Harada S., "Wafer sawing process characterization for thin die applications," *Electronics ManufacturingTechnology Symposium*, vol. 5, pp. 74–77, 2004.

[3] Udo K. and Volker F., "Laser micromachining," tech. rep., Fraunhofer Institute for Material and Beam Technology (IWS), 2011.

[4] Krzysztof L. and Nowakowski A., *Laser beam interaction with materials for microscale applications.* PhD thesis, University of Croatia, 2005.

[5] Craciun V., "Comment on evidence for phase explosion and generation of large particles during high power nanosecond laser ablation of silicon.," *Applied Physics Letters*, vol. 79, pp. 442–443, 2001.

[6] Bosse L. and Bayer A., "Laser applications in microtechnology," *Journal of Material Processing Technology*, vol. 167, pp. 494–498, 2005.

[7] Yilbas B. S., "Laser cutting quality assessment and thermal efficiency analysis," *Journal of Materials Processing Technology*, vol. 155, pp. 2106–2115, 2004.

[8] Gross T. S., Hening S. D., and Watt D. W., "Crack formation during laser cutting of silicon," *Journal of Applied Physics*, vol. 69, pp. 982–990, 1991.

[9] Meung J. K. and Jingwei Z., "Finite element analysis of evaporative cutting with a moving high energy pulsed laser," *Applied Mathematical Modelling*, vol. 25, pp. 203–220, 2001.

[10] Zhigilei L. and Leveugle E., “Computer simulations of laser ablation of molecular substrates,” tech. rep., University of Virginia, 2003.

[11] Steen W. M., “Light industry: an introduction to laser processing and its industrial applications,” *Advances in Laser Materials Processing Technology, Research and Applications*, vol. 1, pp. 44–56, 2010.

[12] Ready J. F., *Industrial Application of Lasers.* Academic Press, 1997.

[13] Steen W.M., *Laser Material Processing.* Springer-Verlag, 1991.

[14] Duarte F. J., “Tunable laser optics,” in *Elsevier Academic, Newyork*, 2003.

[15] Olson R. W. and Swope W. C., “Laser drilling with focused gaussian beams,” *Journal of Applied Physics*, vol. 72, pp. 3686–3696, 1992.

[16] Pronko P., “Thermophysical effects in laser processing of materials with picosecond and femtosecond pulses,” *Journal of Applied Physics*, vol. 78, pp. 6233–6240, 1995.

[17] Ueda T., Yamada K., Oiso K., and Hosokawa A., “Thermal stress cleaving of brittle material by laser beam,” *CIRP Annals Manufacturing Technology*, vol. 51, pp. 149–152., 2002.

[18] Patil R. H., “Thermal modeling of laser drilling and cutting of engineering materials,” Master’s thesis, University of Pune, 2005.

[19] Liu J., Gang D., Liang Z., and Yanbei C., “Numerical study on thermal stress cutting of silicon wafer using two-point pulsed laser,” *Optica Applicata*, vol. 41, pp. 247–255, 2011.

[20] Zhang C., Salama A., and Quick R., “Modelling of microvia drilling with a nd:yag laser,” *Optica Applicata*, vol. 39, pp. 3910–3915, 2006.

[21] Dahotre N. and Harimkar S., “Laser fabrication and machining of materials,” *Springer Science*, vol. 31, pp. 204–210, 2008.

[22] Chwan H. and Sheng C., “Fracture mechanism of laser cutting with controlled fracture,” *Journal of Manufacturing Science and Engineering*, vol. 125, pp. 519–528, 2003.

[23] Gobet M., Obi S., Pavius M., and Takano M., “Implementation of short pulse lasers for wafer scribing and grooving applications,” *Journal of Laser Micro/nanoengineering*, vol. 5, pp. 16–20, 2010.

[24] Richerzhagen B., Delacrtaz G., and Salathe R., “Complete model to simulate the thermal defocusing of a laser beam focused in water,” *Optical Engineering*, vol. 35, pp. 11–16, 1996.

[25] Boyd V., Hunter H., and Keng H., “Understanding high power fiber optic laser beam delivery,” *Journal of Laser Applications*, vol. 19, pp. 210–219, 1996.

[26] Kar A. and Mazumder J. J., “Two-dimensional model for laser induced materials damage due to melting and vaporisation during laser irradiation,” *Journal of Applied Physics*, vol. 68(8), pp. 3884–3891, 1990.

[27] Cebeci T., *Convective Heat Transfer.* Springer, 2002.

[28] Cheng F., Tsui Y. C., and Clyne T. W., “Application of 3d heat flow model to treat laser drilling of carbon fiber composites,” *Acta Metall. Et Mater*, vol. 46, pp. 4273–4285, 1998.

[29] Voisey K. T. and Clyne T. W., “Laser drilling of cooling holes through plasma sprayed thermal barrier coatings,” *Surface and Coating Technology*, vol. 176, pp. 296–306, 2004.

[30] Mazumder J. and Steen W. M., "Heat transfer model for cw material processing," *Journal of Applied Physics*, vol. 51(2), pp. 941–947, 1980.

[31] Modest M. F., *Radiative Heat Transfer.* McGraw Hill, 1993.

[32] Yu L., "Three dimensional finite element method of laser cutting," *Journal of Materials Processing Technology*, vol. 63, pp. 637–639, 1997.

[33] *http://www.ansys.com*, 2008.

[34] Bianco N., Manca O., Nardini S., and Tamburrino S., "Transient heat conduction in solids irradiated by a moving heat source," *Proceedings of theCOMSOL Users Conference*, 2006.

[35] Bianco N., Manca O., Nardini S., and Tamburrino S., "Transient heat conduction in semi-infinite solids irradiated by a moving heat source," *Proceedings of the COMSOL Users Conference*, 2007.

[36] *http://www.comsol.com*, 2008.

[37] Meung J., "3d finite element analysis of evaporative laser cutting," *Applied Mathematical Modelling*, vol. 29, pp. 938–954, 2005.

[38] Miotello A., "Critical assessment of thermal models for laser sputtering at high fluences," *Applied Physics Letter*, vol. 67, pp. 3535–3537, 1995.

[39] Sokolowski K., Bialkowski J., and Vonderlinde k., "Ultrafast laser induced order-disorder transitions in semiconductors," *Physics Revision*, vol. 51, pp. 14186–14198, 1995.

[40] Jiwang Y., Tooru A., and Tsunemoto K., "Response of machining damaged single-crystalline silicon wafers to nanosecond pulsed laser irradiation," *Semiconductor Science and Technology*, vol. 22, pp. 392–395, 2007.

[41] Brock L.M., "Effects of thermoelasticity and a von mises condition in rapid steady-state quasi-brittle fracture.," *International Journal of Solids and Structures*, vol. 33 (28), pp. 4131–4142., 1996.

[42] Gospavic R. and Popov V., "Modeling of laser material interaction using semi analytical approach," *Mathematics and Computers in Simulation*, vol. 65, pp. 211–219, 2004.

[43] Driel H., "Physical electronics," *Physical Review*, vol. 35, pp. 8166–8189, 1987.

[44] Chen J. K. and Tzou D. Y., "Investigation of ultrashort laser damage in semiconductors," *International Journal of Heat and Mass Transfer*, vol. 48, pp. 501–509, 2005.

[45] Lorazo P., Lewis L., and Meunier M., "Picosecond pulse laser ablation of silicon: a molecular dynamics study," *Applied Surface Science*, vol. 168, pp. 276–279, 2000.

[46] Yilbas B. S., "Electron kinetic theory approach-one and three dimensional heating with pulsed laser," *International Journal of Heat and Mass Transfer*, vol. 44, pp. 1925–1936, 2001.

[47] Oane M., Morjan I., and Medianu R., "Thermal fields in multi-mode laser-metallic thin film interaction," *Optics and Laser Technology*, vol. 36, pp. 677–687, 2004.

[48] Oane M. and Sporea D., "Study of heat transfer in ir optical," *Infrared Physics andTechnology*, vol. 42, pp. 31–41, 2001.

[49] Yilbas B. S., Gbadebo S. A., and Sami M., "Laser heating: an electro-kinetic theory approach and induced thermal stresses," *Optics and Laser Engineering*, vol. 33, pp. 65–79, 2000.

[50] Oane M., Morjan I., and Medianu R., "The role of surface absorption coefficient in the thermal field of the laser-thin film interaction," *Optics and Laser Technology*, vol. 36, pp. 677–689, 2004.

[51] Cheng B. and Zhang S., "The effect of interface resistances on thermal wave propagation in multi-layered samples," *Journal of Applied Physics*, vol. 30, pp. 1447–1456, 1997.

[52] Masayoshi Y., Nambu K., and Yamamoto K., "Nonlinear heat equation in a two layer structure," *Journal of Applied Physics*, vol. 57, pp. 965–976, 1985.

[53] Wang Z., Sugioka K., Hanada Y., and Midorikawa K., "Optical waveguide fabrication and integration with a micro-mirror inside photosensitive glass by femtosecond laser direct writing," *Applied Physics*, vol. 88, pp. 699–704, 2007.

[54] Nolte S., Momma C., and Jacobs H., "Ablation of metals by ultrashort laser pulses," *Journal of the Optical Society of America*, vol. 14, pp. 2716–2722, 1997.

[55] Hutton D. V., *Fundamentals of finite element analysis.* McGraw Hill, 2004.

[56] Chen T. and Darling R., "Parametric studies on pulsed near ultraviolet frequency tripled nd:yag laser micromachining of sapphire and silicon," *Journal of Material Processing Technology*, vol. 169, pp. 214–218, 2005.

[57] Yasa E. and Kruth P., "Investigation of laser and process parameters for selective laser erosion," *Precision Engineering*, vol. 34, pp. 101–112, 2010.

[58] Yang T. S., Manyalibo J. M., Elhadj S., Draggoo V. G., and Bisson S., "Thermal transport on co2 laser irradiated fused silica: in situ measurements and analysis," *Journal of Applied Physics*, vol. 56, pp. 217–234, 2009.